nature physics

Article

https://doi.org/10.1038/s41567-025-03003-7

Tau accelerates tubulin exchange in the microtubule lattice

Received: 9 October 2024

Accepted: 17 July 2025

Published online: 4 September 2025

Check for updates

Subham Biswas[1], Rahul Grover[2], Cordula Reuther[2], Chetan S. Poojari[3,4], Reza Shaebani[3], Shweta Nandakumar[1], Mona Grünewald[1], Amir Zablotsky[5], Jochen S. Hub[3,4], Stefan Diez[2,6,7], Karin John[5] ✉ & Laura Schaedel[1,4] ✉

Microtubules are cytoskeletal filaments characterized by dynamic instability at their tips and a dynamic lattice that undergoes continuous tubulin loss and incorporation. Tau, a neuronal microtubule-associated protein, is well known for its role in stabilizing microtubule tips and promoting microtubule bundling. Here we demonstrate that tau also modulates microtubule lattice dynamics. Although tau lacks enzymatic activity, it significantly accelerates tubulin exchange within the lattice, particularly at topological defect sites. Our findings indicate that tau enhances lattice anisotropy by stabilizing longitudinal tubulin–tubulin interactions while destabilizing lateral ones, thereby enhancing the mobility and annihilation of lattice defects. These results challenge the traditional view of tau as merely a passive stabilizer, revealing its active role in dynamically remodelling the microtubule lattice structure.

Microtubules are an essential filamentous component of the cytoskeleton. They exhibit unique dynamic and mechanical properties owing to their hollow structure, their highly ordered arrangement of tubulin dimer subunits and their dissipative growth dynamics. Traditionally, research has focused on the dynamic behaviour of microtubule tips, whose intrinsic instability facilitates rapid growth and shrinkage[1]. By contrast, the microtubule shaft (often termed 'lattice') was long considered a static structure and, thus, received less attention in studies on the dynamic regulation of microtubules.

Recent discoveries have challenged this view, revealing that the microtubule lattice is far from static. Tubulin dimers continuously incorporate into and dissociate from the lattice, rendering it dynamic[2]. Importantly, this dynamicity endows microtubules with the capacity for self-repair and resilience against mechanical stresses typical in cellular environments, such as bending[3] and friction at crossing points[4,5]. The dynamic turnover within the lattice in the absence of mechanical forces has been attributed to topological defect sites[6–8], which act as focal points for tubulin exchange due to the missing inter-subunit bonds of the surrounding tubulin dimers[2,9]. Although lattice dynamics can occur independently of other cellular factors and are, thus, intrinsic to microtubules, they can be modulated by microtubule-associated proteins (MAPs) such as CLIP-170 (ref. 5), CLASP[10], molecular motors[11–13] and severing enzymes[14].

Tau, a well-studied neuronal MAP, predominantly decorates axonal microtubules[15–17] and is known for its role in microtubule nucleation, bundling and stabilization against depolymerization[18–23]. Although tau's influence on microtubule tip dynamics and microtubule bundling has been extensively studied, its impact on lattice dynamics has not been addressed so far. Tau binds along the length of microtubules, where each tau molecule interacts with multiple tubulin dimers[24]. This suggests that it could substantially affect the stability of the lattice.

In this study, we explore the role of tau in microtubule lattice dynamics. Through a combination of in vitro reconstitution experiments and kinetic Monte Carlo modelling, supported by molecular

[1]Experimental Physics and Center for Biophysics, Saarland University, Saarbrücken, Germany. [2]B CUBE—Center for Molecular Bioengineering, TUD Dresden University of Technology, Dresden, Germany. [3]Theoretical Physics and Center for Biophysics, Saarland University, Saarbrücken, Germany. [4]PharmaScienceHub (PSH), Saarbrücken, Germany. [5]Université Grenoble Alpes, CNRS, LIPhy, Grenoble, France. [6]Cluster of Excellence Physics of Life, TUD Dresden University of Technology, Dresden, Germany. [7]Max Planck Institute of Molecular Cell Biology and Genetics, Dresden, Germany. ✉e-mail: karin.john@univ-grenoble-alpes.fr; laura.aradillazapata@uni-saarland.de

dynamics (MD) simulations, we discover that tau, although it generally stabilizes microtubules, surprisingly accelerates the exchange of tubulin in the microtubule lattice. This exchange occurs predominantly at lattice defect sites, which often delineate distinct lattice configurations. Our results suggest that tau stabilizes longitudinal but destabilizes lateral tubulin dimer–dimer contacts. Through this change in anisotropy, tau effectively promotes the repair of lattice defects by increasing their longitudinal mobility, leading to their mutual annealing or removal from the lattice. Thus, tau does not only act as a passive microtubule stabilizer but also facilitates the active elimination of lattice defects.

Tau enhances tubulin incorporation into the microtubule lattice

We first investigated the influence of tau on tubulin incorporation into the microtubule lattice. We grew dynamic microtubules from guanosine-5′-[(α,β)-methyleno]triphosphate (GMPCPP)-stabilized, surface-attached microtubule seeds using green-labelled GTP-tubulin (Fig. 1a, step I). To inhibit further microtubule tip dynamics, we capped the microtubules with slowly hydrolysable GMPCPP-tubulin (step II). We then incubated the microtubules with red-labelled GTP-tubulin in the presence of 0 nM, 0.5 nM or 20 nM of human 2N4R tau for 15 min (step III). Tau covered the non-stabilized microtubule lattice sparsely and homogeneously, exhibiting rapid diffusive motion and dynamic binding and unbinding on the timescale of a few seconds, as previously described[25] (Fig. 1b and Extended Data Fig. 1). The low concentration of tau in our experiments leads to the rapid diffusion of tau along the microtubules (diffusion coefficient of ~0.2 $\mu m^2 s^{-1}$ and short residence time of ~3.7 s; Extended Data Fig. 1). We chose a relatively low free tubulin concentration of 8 μM to limit the microtubule tip growth during the incorporation step. To visualize the incorporated tubulin, we imaged the microtubules after washing out the free tubulin to reduce the background fluorescence (step IV).

When 20 nM of tau was present during the tubulin incorporation step, we noted extended tubulin incorporation stretches along the microtubules, with median lengths of 1.2 μm compared with 0.7 μm in the absence of tau (Fig. 1c,d (top left), Extended Data Fig. 2 and Methods). Furthermore, the median distance between individual incorporations decreased from 12.4 μm when no tau was present to 6.6 μm in the presence of 20 nM of tau, implying an increased spatial frequency of incorporation events (Fig. 1d, top right). These observations reveal a fourfold increase in tubulin incorporation in the presence of 20 nM of tau compared with the control without tau (Fig. 1d, bottom).

Previously, we found that in the absence of other proteins, lattice dynamics constitute a continuous process[2]. To assess whether tau-stimulated tubulin incorporation also exhibits time dependence, we extended the incubation time with red-labelled GTP-tubulin, supplemented with either 0 nM or 20 nM of tau, from 15 min to 30 min. Our observations revealed markedly longer tubulin incorporation stretches, occasionally spanning the majority of the microtubule length (Fig. 1e,f, left). Although we also noted a higher spatial frequency of tubulin incorporation in the absence of tau after 30 min, the presence of 20 nM of tau did not lead to a further increase in the spatial frequency of incorporation stretches (Fig. 1f, middle). This suggests either a limitation in the number of available tubulin incorporation sites (reaching saturation more rapidly in the presence of tau) or an underestimation of these events (due to extensive, overlapping incorporation stretches). Nevertheless, the trend of tau inducing a significant overall increase in tubulin incorporation remains consistent, with approximately 30% of the microtubule lattice showing tubulin incorporation in the presence of 20 nM of tau after 30 min (Fig. 1f, top right). Taken together, tau notably enhances tubulin incorporation into the microtubule lattice during an interaction time of up to 30 min.

Tau stimulates tubulin exchange at defect sites

The lattice of a microtubule is never fully homogeneous; it inherently contains a variety of conformational changes[9], resulting in the emergence of topological defects that mark, for example, protofilament transitions and seam dislocations[2,6–8]. These defects weaken the microtubule lattice by disrupting local tubulin interactions and—as we previously showed—probably drive lattice dynamics[2,3]. To investigate if tau enhances tubulin incorporation specifically at defect sites, we conducted tubulin incorporation experiments in the presence of tau (incubation time of 15 min) and subsequently imaged the microtubules in tubulin-free buffer until fracture (Fig. 2a). Our observations reveal that although incorporation stretches covered only about 20% of the lattice, around 40% of fracture events occurred at these stretches (Fig. 2b). To exclude a possible influence of the fluorescent label used for visualizing the microtubules or the interface between different fluorescent labels on the fracture behaviour, we repeated the experiment using unlabelled microtubules imaged by interference reflection microscopy, which yielded quantitatively comparable results (Fig. 2c and Extended Data Fig. 3). Moreover, we frequently observed the

Fig. 1 | Tau enhances tubulin incorporation into the microtubule lattice. **a**, Experimental setup to assess tubulin incorporation into the microtubule lattice in the presence of tau. First, dynamic microtubules were grown from GMPCPP-stabilized, surface-attached seeds in the presence of green-labelled GTP-tubulin (step I). Then, the microtubules were capped with GMPCPP-tubulin to prevent further microtubule tip dynamics (step II). The microtubules were then incubated with 0 nM, 0.5 nM, or 20 nM of unlabelled tau (black–white circles) and red-labelled GTP-tubulin for 15 min or 30 min (step III). The solution was replaced with a buffer supplemented with Taxol (step IV) to remove excessive background fluorescence, reveal tubulin incorporation sites (yellow star) and keep microtubules stable for imaging. **b**, 20 nM of GFP-labelled tau (shown in magenta) homogeneously coats the microtubule lattice (seed and elongation labelled with 30% and 10% Atto-565, respectively; shown in green) before capping, with the exception of the GMPCPP-stabilized seed. Scale bar, 3 μm. **c**, Example images of microtubules (green) showing incorporation stretches (red, stars) after 15 min in the presence of 0 nM, 0.5 nM and 20 nM of tau. Graphs on the right show the fluorescence profile plots of the red channel. Scale bars, 5 μm. **d**, Top left: lengths of tubulin incorporation stretches increase in the presence of tau. Thick lines represent the medians. $P = 0.033$, $P < 0.0001$ and $P < 0.0001$ for 0 nM versus 0.5 nM, 0.5 nM versus 20 nM and 0 nM versus 20 nM, respectively. Top right: distances between incorporation stretches decrease in the presence of tau. Thick lines represent the medians. $P < 0.0001$, $P = 0.0023$ and $P < 0.0001$ for 0 nM versus 0.5 nM, 0.5 nM versus 20 nM and 0 nM versus 20 nM, respectively. Middle: table showing the median values and interquartile ranges (IQRs) of the incorporation lengths L_{inc} and distances between the incorporation stretches D_{inc}. n denotes the number of analysed incorporation stretches. Bottom: tubulin incorporation is observed along 4.86% of the microtubule lattice at 0 nM of tau, 11.38% at 0.5 nM of tau and 19.14% at 20 nM of tau. Statistics: two-sided Mann–Whitney test. **e**, Example images of microtubules (green) showing incorporation stretches (red, stars) after 30 min in the presence of 0 nM and 20 nM of tau. Graphs on the right show the fluorescence profile plots of the red channel. Scale bars, 5 μm. **f**, Left: incorporation lengths after 15 min versus 30 min of incubation with red tubulin, for 0 nM and 20 nM of tau. Black lines represent the medians. $P < 0.0001$, $P < 0.0001$ and $P = 0.0001$ for 0 nM–15 min versus 0 nM–30 min, 20 nM–15 min versus 20 nM–30 min and 0 nM–30 min versus 20 nM–30 min, respectively. Middle: distances between incorporation stretches after 15 min versus 30 min of incubation with red tubulin, for 0 nM and 20 nM of tau. Black lines represent the medians. $P = 0.0015$, 0.0672 and $P = 0.0128$ for 0 nM–15 min versus 0 nM–30 min, 20 nM–15 min versus 20 nM–30 min and 0 nM–30 min versus 20 nM–30 min, respectively. Top right: tubulin incorporation was observed along 18.13% of the microtubule lattice for 0 nM of tau and 30.59% for 20 nM of tau. For each condition, >2,200 μm of the microtubule length was analysed from $N = 3$ independent experiments. Bottom right: table showing the median values and IQRs of the data presented in the graphs. n denotes the number of analysed incorporation stretches. Statistics: two-sided Mann–Whitney test.

https://doi.org/10.1038/s41567-025-03003-7

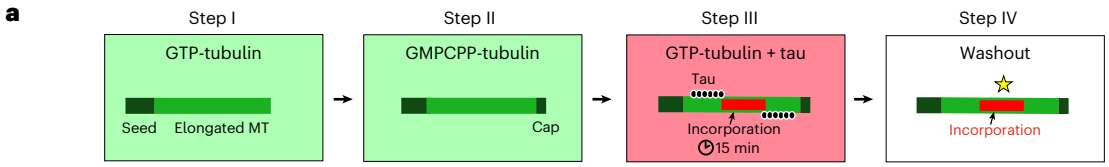

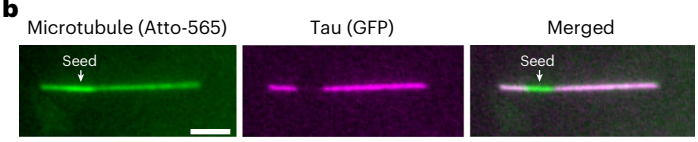

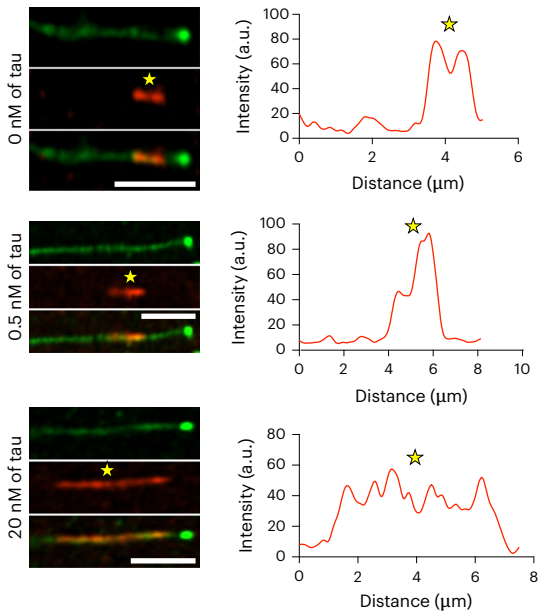

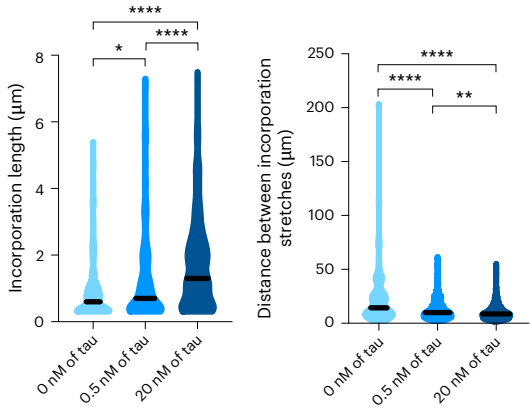

[tau]	L_{inc} (μm)	D_{inc} (μm)	*n*
0 nM	0.7 (0.3 – 1.0)	12.4 (6.4 – 25.5)	126
0.5 nM	0.8 (0.4 – 1.8)	8.4 (5.1 – 14.9)	187
20 nM	1.2 (0.6 – 2.3)	6.6 (4.2 – 11.2)	249

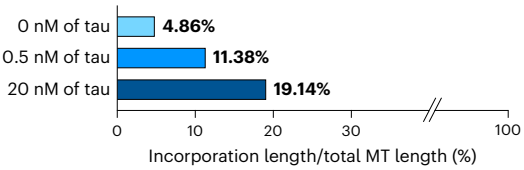

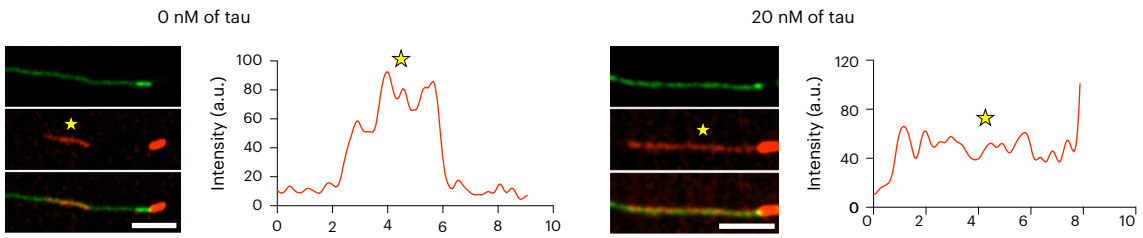

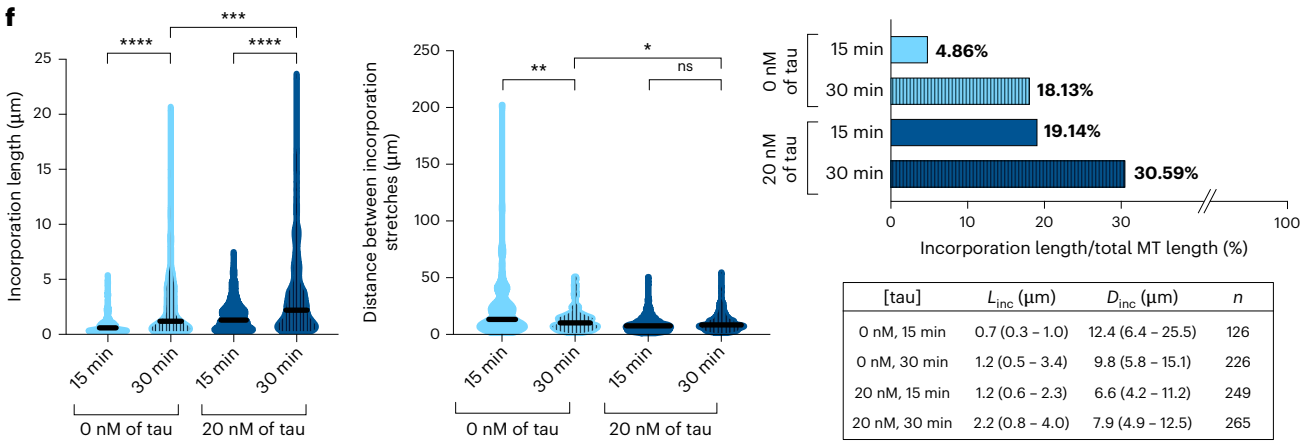

[tau]	L_{inc} (μm)	D_{inc} (μm)	*n*
0 nM, 15 min	0.7 (0.3 – 1.0)	12.4 (6.4 – 25.5)	126
0 nM, 30 min	1.2 (0.5 – 3.4)	9.8 (5.8 – 15.1)	226
20 nM, 15 min	1.2 (0.6 – 2.3)	6.6 (4.2 – 11.2)	249
20 nM, 30 min	2.2 (0.8 – 4.0)	7.9 (4.9 – 12.5)	265

disappearance of incorporation stretches before microtubule fracture (Fig. 2d). This suggests that tau-enhanced tubulin incorporation indeed occurs preferentially at pre-existing lattice defect sites.

We then asked if tubulin incorporation goes along with tubulin exchange in the microtubule lattice, that is, if tubulin from the solution replaces pre-existing tubulin in the original lattice or if tubulin from solution is just 'added' to the pre-existing lattice. When plotting the fluorescence intensities along individual microtubules, the original (green) lattice signal often appeared to slightly decrease at stretches of newly incorporated (red) tubulin, both in the presence and absence of tau (Fig. 2e). A thorough quantification of this effect, which is a direct readout of lateral tubulin loss (Methods), showed a reduction in the lattice fluorescence intensity by approximately 7%–15% (corresponding to a tubulin loss across one to two protofilaments), with a more pronounced reduction after 30 min than after 15 min (Fig. 2f). We then estimated the amount of incorporated tubulin by normalizing the fluorescence intensity of the red-labelled incorporation stretches to the fluorescence intensity of red-labelled microtubule tips grown in the presence of GTP (Fig. 2g; for 30-min incubation time with red tubulin, see Methods), which typically corresponded to intensities expected from one to two protofilaments, occasionally reaching up to four. In particular, the amount of incorporated tubulin per length of microtubule was lower in the presence of tau. Overall, our findings imply that (1) the incorporated tubulin does indeed replace tubulin from the original lattice; (2) only a small portion of the lattice is exchanged; and (3) that although the longitudinal extent of incorporation (incorporation length) increases in the presence of tau (Fig. 1), the lateral extent of incorporation decreases in the presence of tau (Fig. 2g).

Tau slows down microtubule fracture

The overall enhanced longitudinal incorporation of tubulin in the presence of tau (Fig. 1) may either be ascribed to an elevated effective tubulin on-rate at the lattice (as demonstrated for the MAP CLASP[10]) or to increased tubulin loss from the lattice followed by the subsequent incorporation of new tubulin (that is, self-repair, a phenomenon observed, for example, for molecular motors[11–13] and severing enzymes[14]). To distinguish between these two possibilities, we examined microtubule fracture as a result of tubulin loss. We grew capped microtubules (Fig. 3a, steps I and II) and then imaged them in the presence of 0 nM or 20 nM of tau, but without free tubulin (steps III and IV). Figure 3b shows an example image sequence of a microtubule fracture event. We found that tau significantly slowed down microtubule fracture compared with the control without tau (Fig. 3c), implying that tau does not cause increased tubulin loss.

Tau increases lattice anisotropy

The slowdown of microtubule fracture in the presence of tau indicates an increased lattice stability compared with the control case. However, when inspecting the longitudinal damage extension before fracture, we found that tau considerably increased the size of damage compared with the case without tau (Fig. 4a,b). Such enhanced growth of longitudinal damage size in the presence of tau can only be reconciled with an increased survival time when lateral fracture propagation across protofilaments is, at the same time, slowed down relative to longitudinal propagation. This reasoning prompts the following thought experiment: if the microtubule lattice was isotropic, damage would spread laterally and longitudinally at the same speed (Fig. 4c, left). Assuming that fracture occurs when all protofilaments are damaged at any given position along the microtubule, the expected damage size at fracture would be about 13 dimers in all directions. By contrast, in an anisotropic lattice, where longitudinal inter-dimer bonds are stronger than lateral ones, the damage would spread faster in the longitudinal direction compared with the lateral direction, leading to an increased longitudinal damage size at fracture (Fig. 4c, right). We, therefore, propose that the damage geometry, that is, the observed longitudinal damage size, is a direct readout of lattice anisotropy. In our experiments, the observed longitudinal damage sizes, both in the absence and presence of tau, are well above 1 µm (Fig. 4b; substantially longer than the length of 13 tubulin dimers with a size of 8 nm each), indicating an anisotropic microtubule lattice with stronger longitudinal than lateral bonds. The longer extensions of the damage sizes observed in the presence of tau compared with the case without tau (Fig. 4a,b) indicate that tau strengthens the longitudinal bonds even further.

Indeed, a recent high-resolution cryo-electron microscopy study revealed that tau's microtubule-binding domains bind along individual protofilaments, each bridging an intra- and an inter-dimer contact, potentially strengthening longitudinal tubulin interactions[24]. To test this, we performed coarse-grained (CG) molecular dynamics (MD) simulations of a tau microtubule-binding domain on three longitudinally connected alpha-/beta-tubulin monomers and used umbrella sampling (US) to compute the free-energy profile along the dissociation of a longitudinal dimer–dimer contact (Fig. 4d). Here the free-energy

Fig. 2 | Tau stimulates tubulin exchange at defects. a, Experimental setup to visualize microtubule fracture after tubulin incorporation. Microtubules were grown with green-labelled tubulin (step I) and capped (step II) before incubation with 20 nM of tau and red-labelled tubulin (step III). Then, the solution was replaced with a buffer without Taxol (step IV) and immediately imaged for 50 min (step V). **b**, Left: example images showing a microtubule that developed a kink (arrow) at an incorporation stretch (red, star) before fracture at this site. Scale bar, 3 µm. Right: microtubule fracture occurred more frequently at tubulin incorporation sites than is to be expected based on incorporation lengths compared with the total microtubule length. Here 26 microtubules were analysed in three independent experiments. For additional data with unlabelled microtubules, see Extended Data Fig. 3. **c**, Left: example images showing a label-free microtubule (imaged with interference reflection microscopy) developing a kink (white arrow) at an incorporation stretch (red, star, imaged with wide-field fluorescence microscopy) in the absence of free tubulin before fracture. Scale bar, 3 µm. The corresponding image sequence is shown in Extended Data Fig. 3. Right: microtubule fracture occurred more frequently at tubulin incorporation sites than is to be expected based on incorporation lengths compared with the total microtubule length. Here 25 microtubules were analysed in five independent experiments. **d**, Example images showing that the incorporation stretch (top and bottom panels; red, star) disintegrated before the microtubule developed a kink (top panel, green, arrow) and disassembled. Scale bar, 3 µm. **e**, Example images of tubulin incorporation after 30 min (red, stars) into the microtubule lattice (green), averaged over at least five consecutive time points, with fluorescence profile plots in the absence (left) and presence (right) of 20 nM of tau. Scale bars, 3 µm. **f**, Estimation of the amount of lateral tubulin loss from the lattice. Top: lattice fluorescence at incorporation stretches is normalized to the fluorescence of the lattice next to the incorporation stretches (Methods). Bottom: normalized lattice fluorescence in the absence and presence of 20 nM of tau after 15- and 30-min incorporation time. For a lattice with 13 protofilaments, a normalized fluorescence of 0.85 corresponds to a lateral tubulin loss over two protofilaments. Black lines represent the medians. $P = 0.0076$ and $P = 0.0082$ for 0 nM–15 min versus 0 nM–30 min and 20 nM–15 min versus 20 nM–30 min, respectively. Three different experiments were analysed per condition. The table shows the median intensities and IQRs. *n* denotes the number of analysed incorporation stretches. Statistics: two-sided unpaired *t*-tests. **g**, Estimation of the amount of lateral tubulin incorporation into the lattice. Top: example image of an incorporation stretch (star) and the microtubule tip consisting of red-labelled tubulin. The fluorescence of incorporated tubulin at incorporation stretches is normalized to the fluorescence of the tip (Methods). Scale bar, 3 µm. Bottom: normalized incorporation fluorescence in the absence and presence of 20 nM of tau. For a 13-protofilament lattice, a normalized fluorescence intensity of 0.15 corresponds to lateral tubulin incorporation over two protofilaments. Black lines represent the medians. Three different experiments were analysed per condition. $P = 0.0012$ (two-sided Mann–Whitney test). The table shows the median intensities and IQRs. *n* denotes the number of analysed incorporation stretches.

https://doi.org/10.1038/s41567-025-03003-7

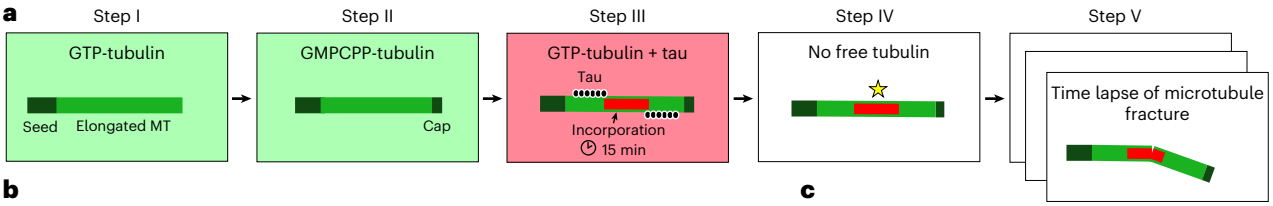

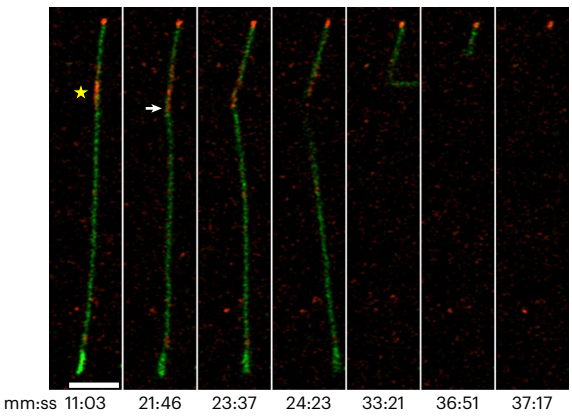

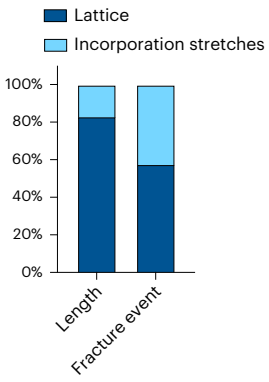

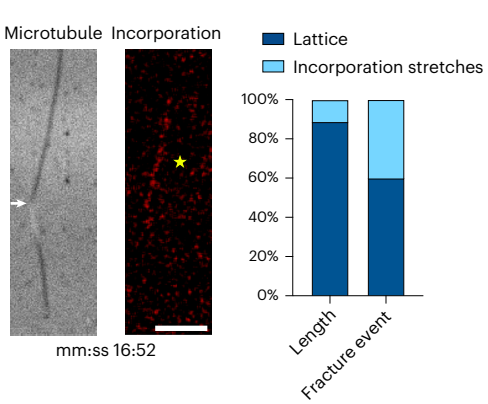

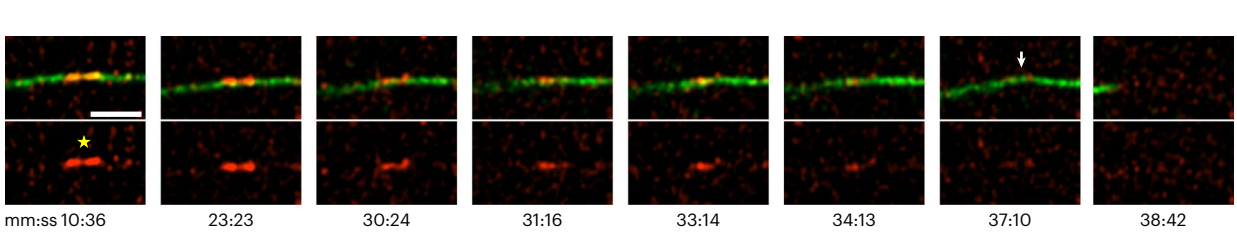

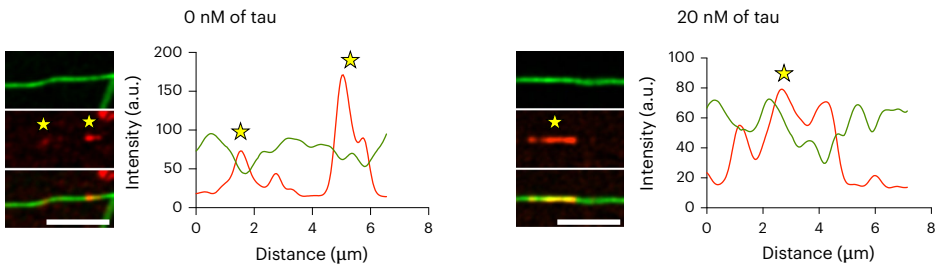

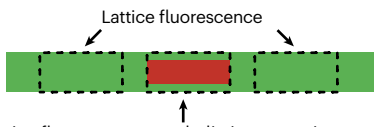

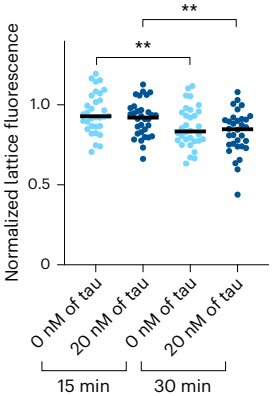

[tau]	I_{fluor}	n
0 nM, 15 min	0.93 (0.86 – 1.05)	32
20 nM, 15 min	0.92 (0.82 – 0.98)	32
0 nM, 30 min	0.83 (0.78 – 0.96)	32
20 nM, 30 min	0.85 (0.74 – 0.91)	32

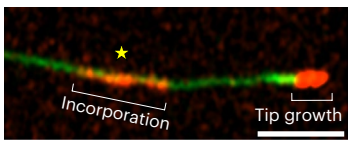

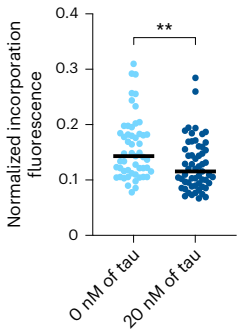

[tau]	I_{fluor}	n
0 nM	0.15 (0.12 – 0.18)	53
20 nM	0.12 (0.09 – 0.16)	57

https://doi.org/10.1038/s41567-025-03003-7

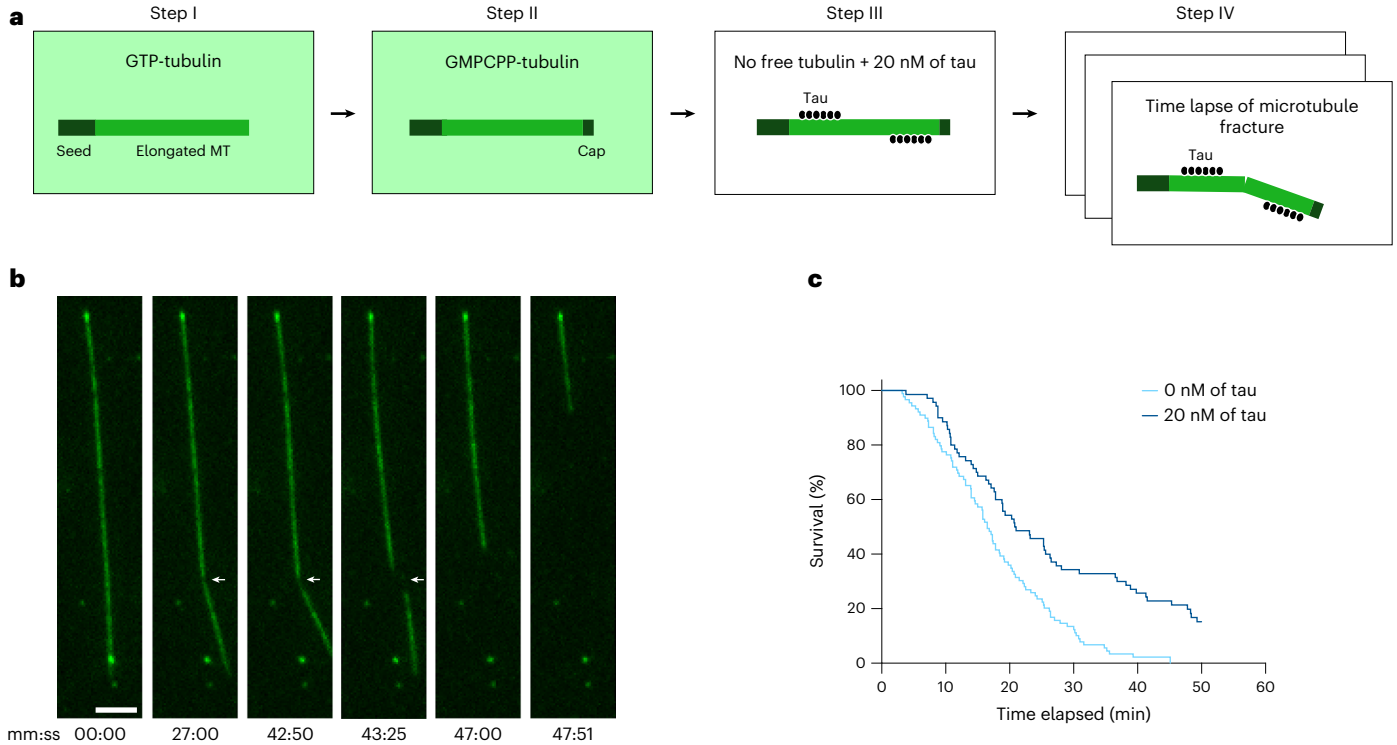

Fig. 3 | Tau stabilizes microtubules against fracture. a, Experimental setup to quantify microtubule fracture in the absence of free tubulin. Microtubules were grown with GTP-tubulin (step I) and capped with GMPCPP-tubulin (step II). Then, they were incubated with or without 20 nM of tau in the absence of free tubulin (step III) and immediately imaged for 50 min (step IV). **b**, Image sequence showing a microtubule developing a damaged region, which is visible due to reduced green fluorescence (arrow) resulting from the loss of tubulin from the lattice. The microtubule eventually broke along the softened region and disassembled. Scale bar, 3 µm. **c**, Survival curves showing that microtubule survival increases in the presence of tau. For 0 nM of tau, 83 microtubules were analysed in five independent experiments. For 20 nM of tau, 65 microtubules were analysed in four independent experiments. The differences in survival are statistically significant ($P < 0.0001$), based on a log-rank (Mantel–Cox) test.

minimum at a distance of approximately 4 nm corresponds roughly to the known equilibrium state[26–29]. As shown by the difference between the dark and light blue curves in Fig. 4d, the binding free energy is lower in the presence of tau than in its absence. Although the approximations underlying our CG simulations do not permit a precise quantification of the difference in binding free energies with and without tau, they strongly suggest that tau stabilizes longitudinal dimer–dimer contacts, probably affecting lattice anisotropy.

To experimentally investigate the effect of tau on lattice anisotropy, we utilized tubulin incorporation as a readout for the preceding tubulin loss. We incubated capped green microtubules in a tubulin-free buffer for a short duration (5 min) in the presence or absence of tau (Fig. 4e). Subsequently, we introduced red tubulin to allow for self-repair of the lattice sites that experienced tubulin loss. Compared with the microtubule fracture experiments reported above, where the damage size was recorded at the time of complete breakage for each microtubule, here we assessed the microtubule damage at the same time for all microtubules (in the absence and presence of tau). We indeed observed longer tubulin incorporation stretches (Fig. 4g) spanning fewer protofilaments (Fig. 4h) when tau was present in the tubulin-free buffer. Taken together, these results indicate that tau increases lattice anisotropy.

Numerical modelling confirms multiple effects of tau on the microtubule lattice

Thus far, we have experimentally established that tau (1) increases tubulin exchange at the lattice defects; (2) overall slows down microtubule fracture; and (3) increases the lattice anisotropy, suggesting that tau has multiple effects on the microtubule lattice. We, therefore, aimed to determine the most parsimonious explanation for these experimental observations. To that end, we developed a semiquantitative kinetic Monte Carlo model for the microtubule lattice[2,26,30,31] that captures the relevant time- and length scales with a minimum set of parameters (Fig. 5a; the model description in the Supplementary Information provides further details and model parameters). Most importantly, we model the dynamics of monomer vacancies that lead to seam dislocations, which are the most frequent defects in vitro and which may lead to the creation of additional A-lattice contacts (multi-seam structures[8]). On the basis of the available structural information[8], we introduce two distinct types of monomer vacancy, denoted as V_1 and V_2 (Fig. 5a). For V_1-type defects, an existing A-lattice seam undergoes a lateral shift by one protofilament. By contrast, V_2-type defects generate two additional A-lattice seams within a B-lattice, extending either towards the plus or minus end of the microtubule, denoted as V_{2+} and V_{2-}, respectively. Neighbouring dimers interact via bond energies ($\Delta G_1 < 0$ and $\Delta G_2 < 0$ for longitudinal and lateral contacts, respectively) and are defined by the lattice anisotropy $A = \Delta G_1/\Delta G_2$ and the total binding energy $\Delta G_{tot} = 2(\Delta G_1 + \Delta G_2)$. The seam and seam dislocations are characterized by the following properties. (1) Since A-lattice contacts lead to an increased lateral opening between the protofilaments[32] and microtubules exhibiting ectopic A-lattice seams depolymerize at an accelerated rate[33], we assign a weak destabilization $\Delta G_S > 0$ to the lateral A-lattice contacts compared with B-lattice contacts. (2) Seam dislocations induce a sharp shift in the lattice structure on the scale of a few tubulin dimers. In solid mechanics, it is well established that defects distort the lattice structure of highly ordered materials and are associated with a non-local stress field for various systems ranging from metals[34] to colloidal crystals[35]. Therefore, we assign a weak destabilization $\Delta G_V > 0$ to the dimers around the seam dislocations that we limit to the nearest neighbours for simplicity and which we refer to as the 'defect energy'.

Since the dynamics of tau (for the dwell time and diffusion constant, see Extended Data Fig. 1 and Supplementary Information) is much faster than the lattice dynamics, the presence of tau on the microtubule lattice is modelled by effectively modulating the binding energy (ΔG_{tot}) and lattice anisotropy (A) compared with the bare lattice. The lateral destabilization of A-lattice contacts compared with B-lattice contacts ΔG_S (point (1) above) and the defect energy ΔG_V (point (2) above) are unaffected by tau. To determine the lattice parameters relevant to our experiments, we used numerical simulations (Fig. 5b–e) to replicate the observed fracture behaviour. We found that although stabilizing longitudinal dimer contacts (ΔG_l) increases the damage size at fracture (Fig. 5c), achieving agreement with our experimental data and avoiding an exponential increase in fracture time (Fig. 5d) requires a simultaneous decrease in the stability of lateral contacts. Ultimately, our model (Fig. 5e) reproduces the experimentally observed increase in fracture time (Fig. 3c) and longitudinal damage spreading (Fig. 4b) in the presence of tau by incorporating an increase in lattice anisotropy A from 1.5 to 2.1 and a slight net stabilization of the lattice (−0.2 kT for $\Delta G_{tot} = -36$ kT). Next, we used the two estimated lattice parameter sets (ΔG_{tot} and A) to investigate tubulin incorporation at defect sites with our model. V_1 defects are longitudinally symmetric with respect to the presence of A-lattice contacts (Fig. 5f, top). As continued tubulin loss and incorporation occur, they move mainly diffusively along a protofilament (Extended Data Fig. 4). By contrast, V_2 defects exhibit a mainly ballistic motion due to their longitudinal asymmetry (Fig. 5f (bottom) and Extended Data Fig. 4). Thus, V_2 defects generally produce longer tubulin incorporation stretches than V_1 defects (kymographs in Fig. 5g,h (left)). In our model, in the presence of tau, the incorporation stretches at V_1 and V_2 defect sites are longer than in the absence of tau, which is a direct consequence of the increased lattice anisotropy that favours the loss of dimers adjacent to the defect in the longitudinal direction (Fig. 4c). Note that the accelerated defect dynamics in the presence of tau leads to a small advective bias towards the microtubule plus end. This effect results from the different mechanisms of GTP hydrolysis of the tubulin β-subunit at the microtubule plus and minus ends and manifests itself most importantly for V_1 defects. It is also responsible for a small difference in the propagation speed between V_{2+} and V_{2-} defects, leading to slightly different incorporation lengths at the end of the observation time (Fig. 5h, left).

Finally, we have simulated the incorporation of free tubulin into microtubules with randomly placed defects. The first peak in the histogram of incorporation lengths (Fig. 5h, top right) in the presence of tau at around 0.5 µm can be attributed to V_1 defects, whereas the second peak at around 1.5 µm stems mostly from faster-moving V_2 defects. This bimodal distribution is also present in the experimental data (Fig. 5h, right bottom). These results indicate that tau accelerates lattice dynamics for both V_1 and V_2 defects, leading to longer tubulin incorporation stretches than in the control without tau within the studied observation times.

Taken together, our simple model can explain the multiple effects of tau observed in our experiments when assuming that tau leads to weak stabilization (−0.2 kT) of the perfect microtubule lattice, whereas it considerably enhances the lattice anisotropy from $A = 1.5$ in the absence of tau to $A = 2.1$ in the presence of tau. Moreover, our model recapitulates that the effects of tau on microtubule stability depend on free tubulin levels: it slows down fracture in the absence of free tubulin, yet promotes defect mobility along protofilaments in the presence of free tubulin.

Does tau promote the elimination of defects from the microtubule lattice?

The above-described enhanced defect mobility in the presence of tau is predicted to increase the probability for defects to meet and anneal in a given time interval (Fig. 6a, top). In addition, ballistically moving V_2 defects may propagate until they reach the end of the non-stabilized microtubule, leaving behind a repaired trace (Fig. 6a, bottom). To test this prediction experimentally, we incubated green capped microtubules with unlabelled tubulin in the presence of 0 nM or 20 nM of tau for 30 min to allow defects to anneal or move to the end of the non-stabilized lattice (Fig. 6b, steps I–III). We then incubated the microtubules with red-labelled tubulin in the absence of tau for 15 min (step IV) before washout (step V). Although we found no significant difference in the lengths of incorporation sites, the tau-incubated microtubules showed a significant decrease in the spatial frequency of incorporations (Fig. 6c). Since the chance for defects to travel to the end of the non-stabilized lattice is higher the shorter a microtubule is, we separated our results according to the lengths of the non-stabilized microtubule parts. Indeed, we found a pronounced effect for lengths up to 10 µm in the presence of tau, where the median distance between incorporation sites increased more than twofold from 20.3 µm in the control (without tau) to 51.1 µm (Fig. 6d). Our results, thus, support the model's prediction that tau enhances defect mobility. To further strengthen our conclusions and confirm that defect motion underlies tubulin incorporation, we performed two-colour tubulin incorporation cycles in a separate experiment (Fig. 6e). We incubated far red-labelled capped microtubules (steps I and II) first with green-labelled tubulin

Fig. 4 | Tau increases lattice anisotropy. a, Example image sequence of a microtubule fracture event showing the longitudinal spreading of the damaged region (region of reduced fluorescence, white arrows) in the presence of tau. Scale bar, 3 µm. **b**, Lengths of the damaged lattice regions before fracture are increased in the presence of tau. Five and four different experiments were analysed for 0 nM and 20 nM of tau, respectively. The table shows the medians and IQRs of the lengths of the damaged lattice regions. *n* denotes the number of analysed microtubules. **c**, Left: in an isotropic lattice, the damaged region propagates longitudinally and laterally at the same rate. Right: in an anisotropic lattice with stronger longitudinal than lateral bonds, tubulin loss along the longitudinal direction is favoured. **d**, Tau stabilizes longitudinal dimer–dimer contacts. Free-energy profiles for tubulin dissociation in the presence (dark blue curve) and absence (light blue curve) of tau as a function of the centre-of-mass distance between adjacent monomers. In the presence of tau, the binding affinity along the longitudinal dissociation of tubulin dimer and monomer is stronger than in the absence of tau. The shaded areas represent the standard error of the mean. The inset shows the structure of tau (magenta) interacting with three tubulin monomers (green, top view) with a single monomer depicted in both associated and dissociated states from the microtubule–tau complex. **e**, Experimental setup to confirm that tau reduces tubulin loss in the absence of free tubulin. Microtubules were grown with green-labelled tubulin (step I) and capped (step II). They were then incubated with or without 20 nM of tau in the absence of free tubulin for 5 min (step III), followed by a 15-min incubation step with red-labelled tubulin in the absence of tau (step IV). Microtubules were imaged after the washout of free tubulin (step V). **f**, Example images and fluorescence profile plots showing tubulin incorporation (red, stars) into microtubules (green) after a 5-min incubation step in the absence of free tubulin (without or with 20 nM of tau). Scale bars, 5 µm. **g**, Tubulin incorporation sites are longer (top left; $P < 0.0001$) but equally spaced (top right, $P = 0.4729$) in the presence of 20 nM of tau compared with the control, leading to an overall increase in the microtubule length fraction with tubulin incorporation (bottom). Black lines represent the medians. More than 1,700 µm of microtubule length was analysed in three independent experiments per condition. The table (middle) shows the medians and IQRs from the graphs; *n* denotes the number of analysed incorporation stretches. Statistics: two-sided Mann–Whitney tests. **h**, Estimation of the amount of incorporated tubulin in an incorporation stretch. The normalized fluorescence of incorporated tubulin, as explained in Fig. 2g, is shown here. Three different experiments were analysed for both 0 nM and 20 nM of tau. Black lines represent the medians. $P = 0.0012$ (Mann–Whitney test). The table shows the medians and IQRs; *n* denotes the number of analysed incorporation stretches.

https://doi.org/10.1038/s41567-025-03003-7

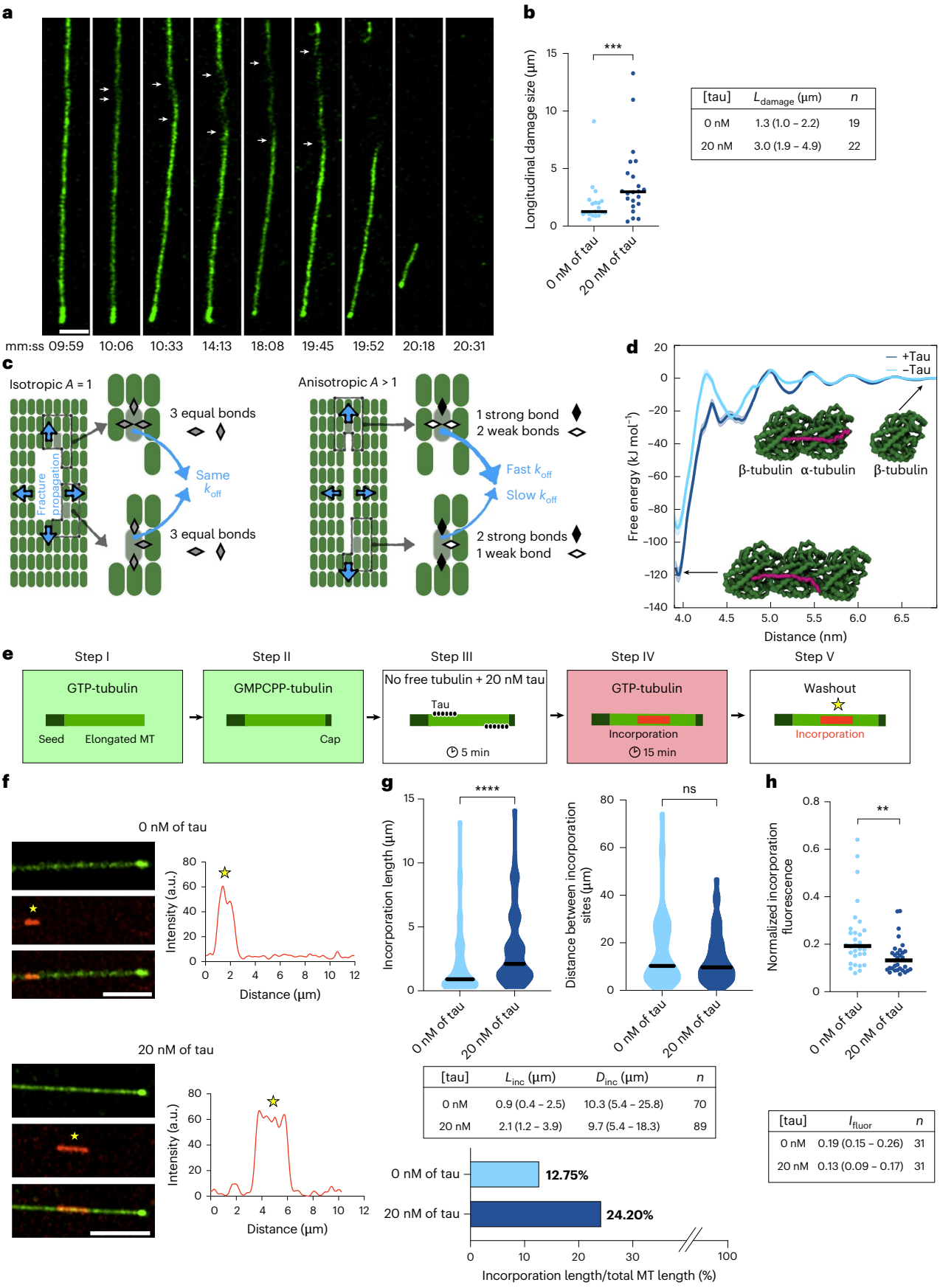

https://doi.org/10.1038/s41567-025-03003-7

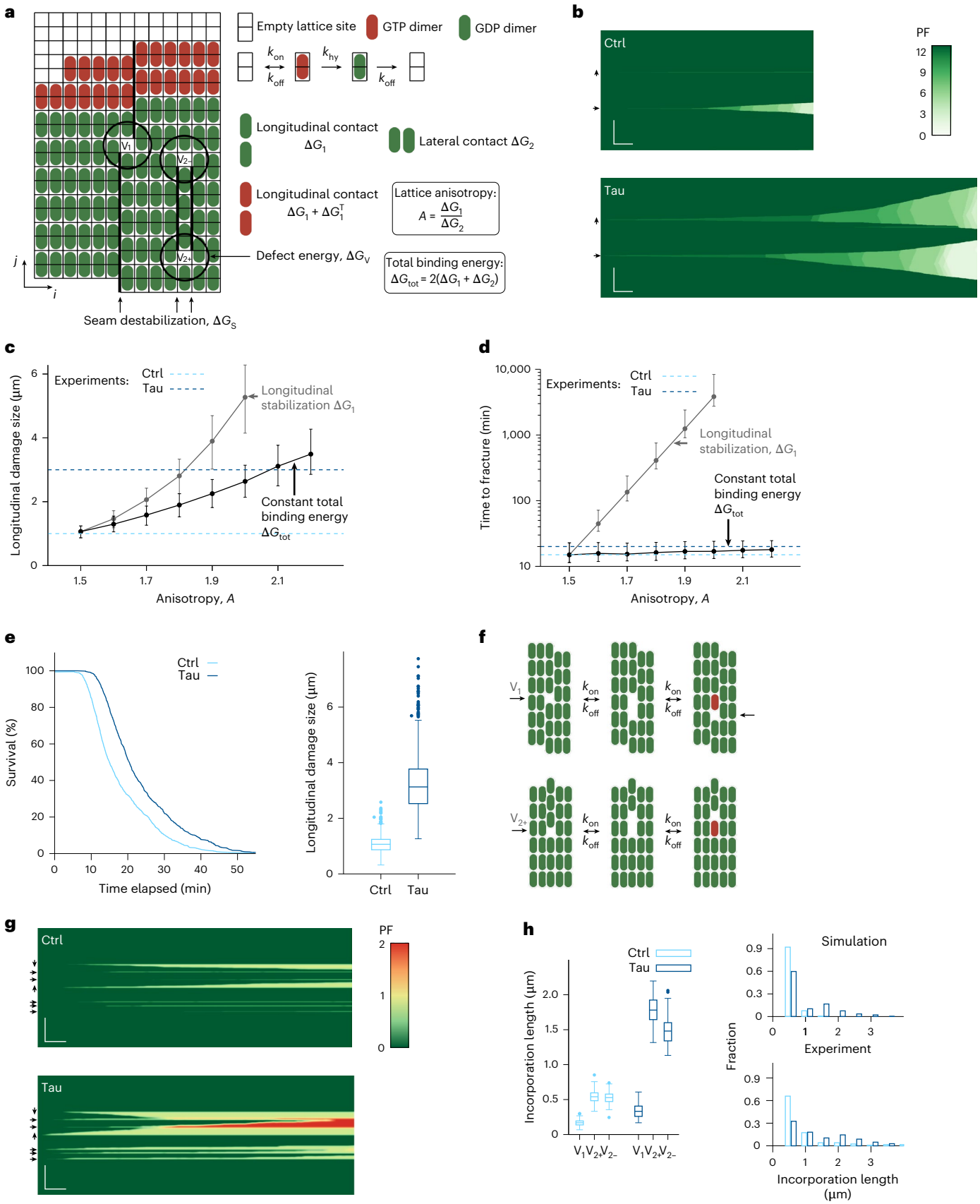

(step III), followed by red-labelled tubulin (step IV), each for 15 min in the presence of tau before washout (step V). We then categorized the observed incorporation stretches into four groups: adjacent (green and red stretches side by side), primary (only green from the first cycle), secondary (only red from the second cycle) and overlapping (overlaid green and red, potentially on neighbouring protofilaments; Fig. 6f and Extended Data Fig. 5). If our model is correct, most incorporations should either show adjacent green and red stretches, indicating

Fig. 5 | Kinetic Monte Carlo model. a, Kinetic Monte Carlo model of a microtubule, depicting the 13-protofilament, three-start helix structure and monomer vacancies (V_1, V_{2+} and V_{2-}), where V_{2+} and V_{2-} denote the seam orientation towards the plus and minus ends, respectively. Kinetic transitions (attachment, detachment and hydrolysis) and energetic contributions (binding energies ΔG_1, ΔG_2, total ΔG_{tot} and anisotropy A, seam destabilization ΔG_S and defect destabilization ΔG_V) govern the dimer detachment kinetics via Kramer's theory. **b**, Simulated kymographs of the fracture of end-stabilized 10-µm-long microtubules in the absence of free tubulin in the absence (top) and presence of tau (bottom). The positions of V_1 and V_{2+} defects are marked by → and ↑ arrows, respectively. Scale bars, 2 µm (vertical); 1 min (horizontal). The colour code indicates the number of intact protofilaments (PF). Parameters are $\Delta G_S = 0.5$ kT, $\Delta G_{tot} = -36$ kT, $A = 1.5$ (absence of tau) and $\Delta G_{tot} = -36.2$ kT, $A = 2.1$ (presence of tau), as indicated in Supplementary Table 2. **c**,**d**, Simulated longitudinal damage size at fracture (**c**) and time to fracture (**d**) depending on the lattice anisotropy A by increasing the longitudinal binding energy ΔG_1 at constant lateral binding energy ΔG_2 and for a constant total binding energy $\Delta G_{tot} = -36$ kT (A increases by longitudinal stabilization and lateral destabilization). The dashed lines indicate the order of magnitude of the longitudinal damage sizes and fracture times measured in the experiments. The total lattice energy in **c** is $\Delta G_{tot} = -36$ kT for $A = 1.5$. The symbols correspond to the medians, and the error bars indicate the IQR. $n = 1{,}000$ for each symbol. **e**, Left: simulated survival curves of end-stabilized microtubules in the absence of free tubulin as well as in the presence (dark blue) and absence (light blue) of tau. The curves show the survival of $n = 1{,}000$ microtubules of 10-µm length with randomly placed defects (frequency, 0.15 µm^{-1}; Supplementary Information). Right: simulated longitudinal damage size at complete microtubule fracture (that is, when damage laterally spans 13 protofilaments). Dark (light) blue denotes the simulations with (without) tau. Horizontal lines and boxes indicate the medians and IQRs. Whiskers extend to the most distant point whose value lies within 1.5 times the IQR. Points lying outside the whiskers are drawn individually. **f**, Schematic of defect motion via dimer detachment and attachment. Propagation of V_1 and V_{2+} defects is indicated by the horizontal grey arrows. **g**, Simulated kymographs of dimer attachment (incorporation) dynamics into end-stabilized microtubules. The positions of V_1, V_{2+} and V_{2-} defects are marked by →, ↑ and ↓ arrows, respectively. Scale bars, 2 µm (vertical), 1 min (horizontal). The colour code indicates the number of exchanged protofilaments. Parameters are the same as indicated in **b**, with $\Delta G_V = 1.25$ kT (Supplementary Table 2). To compare the simulated results with experiments, the longitudinal positions of the incorporated dimers were convoluted with a point spread function (Supplementary Information). **h**, Length and frequency of incorporation stretches. Left: incorporation length depending on the defect type (V_1, V_{2+} and V_{2-}) in the presence of tau (dark blue) compared with the control in the absence of tau (light blue) after 15 min. The sample size is $n = 100$ for each defect type and condition. Horizontal lines and boxes indicate the medians and IQRs. Whiskers extend to the most distant point whose value lies within 1.5 times the IQR. Points lying outside the whiskers are drawn individually. Top right: simulated distribution of incorporation lengths (>300 nm to match the experimental limit of detecting incorporations; Supplementary Information) after 15 min in the presence (dark blue) and absence (light blue) of tau for $n = 1{,}000$ microtubules of 10 µm length with randomly placed defects (frequency, 0.15 µm^{-1}; Supplementary Information), showing a bimodal distribution in the presence of tau. Bottom right: experimental distribution of incorporation lengths. The data correspond to those shown in Fig. 1d.

a moving defect, or only green stretches, suggesting that the defect annealed with another or reached the end of the non-stabilized microtubule segment within the first 15 min. Strikingly, 50% of the observed incorporations show adjacent green and red stretches, whereas 25% contained only green from the first cycle (Fig. 6g). An additional 14% showed overlapping stretches. In 11% of cases, we observed only red stretches, which may reflect diffusively moving defects that erased the green stretches from the first cycle. These results strongly support the idea that tau-driven defect mobility promotes the elimination of defects from the microtubule lattice.

Figure 6h illustrates our current understanding of tau-induced modifications in the microtubule lattice and its consequences on tubulin turnover. Our experimental findings reveal that tau enhances lattice anisotropy and provides a slight stabilization against microtubule fracture. MD and kinetic Monte Carlo simulations strongly indicate that this increased anisotropy results from the strengthening of longitudinal and concurrent weakening of lateral inter-dimer contacts, leading to only a modest overall stabilization of the intact lattice. In particular, this change in anisotropy accelerates the longitudinal movement of topological lattice defects, thereby increasing tubulin turnover.

The proposed modifications in tubulin bond energies by tau align with the previous descriptions of tau slowing down microtubule depolymerization[20] and may also account for the previously observed increase in microtubule stiffness in the presence of tau[36–40].

Interestingly, a recent study reported that tau increases the number of lattice defects when present during microtubule polymerization[23].

Fig. 6 | Tau increases defect mobility. a, Example representation of the elimination of two V_1 lattice defects via annealing (top) and a V_{2+} defect via motion up to the microtubule extremity (bottom). **b**, Experimental setup to visualize tubulin incorporation after an initial 30-min tubulin incorporation step in the presence or absence of tau. Microtubules were grown with green-labelled tubulin (step I) and capped (step II) before incubation with unlabelled tubulin in the presence or absence of 20 nM of tau for 30 min (step III). This initial incorporation step was followed by an additional 15-min incorporation step in the presence of red-labelled tubulin and in the absence of tau (step IV) before washout and imaging (step V). **c**, Incorporation lengths (top left, $P = 0.2715$) and distances between incorporation stretches (top right, $P = 0.0015$). Black lines represent the median. Orange lines represent the median values from Fig. 1d (incorporation length and distance between incorporations for 0 nM of tau) as reference. The resulting tubulin incorporation lengths are comparable between the samples, but the control sample shows slightly more frequent tubulin incorporations (>3,000 µm of microtubule length was analysed from three independent experiments per condition). Bottom: table showing the median values and IQRs from the graphs. n denotes the number of analysed incorporation stretches. Statistics: two-sided Mann–Whitney tests. **d**, Top: distances between tubulin incorporation stretches from the graph on the left were binned according to the microtubule length, showing a marked increase for short (0–10 µm) microtubules in the presence of tau. Black lines represent the median. The orange line represents the median from Fig. 1d (distance between incorporation stretches for 0 nM of tau) as reference. $P = 0.3664$ and $P < 0.0001$ for 0 nM and 0–10 µm versus 0 nM and >10 µm, and 20 nM and 0–10 µm versus 20 nM and >10 µm, respectively (two-sided Mann–Whitney tests). Bottom: table showing the median values and IQRs from the graph. n denotes the number of analysed incorporation stretches. **e**, Experimental setup to visualize tubulin incorporation in two consecutive cycles. Microtubules were grown with far red-labelled tubulin (step I) and capped (step II) before incubation with green-labelled tubulin in the presence of 20 nM of tau for 15 min (step III). This first incorporation cycle was followed by a second 15-min incorporation cycle in the presence of red-labelled tubulin and 20 nM of tau (step IV) before washout and imaging (step V). **f**, Classification of tubulin incorporation in four different groups: adjacent, primary (first cycle only), secondary (second cycle only) and overlapping (overlaying stretches). Scale bars, 5 µm. For further examples of dual-colour tubulin incorporation, see Extended Data Fig. 5. **g**, Quantification of 468 incorporation stretches from three samples. **h**, Conceptual model of the multiple effects of tau on microtubule lattice dynamics. On the basis of our experimental results and numerical simulations, we propose a model in which tau increases the anisotropy of tubulin bond energies in the lattice by strengthening longitudinal bonds and weakening lateral bonds. Overall, tau has a stabilizing effect on the intact lattice, which is consistent with the previously observed reduction in the microtubule depolymerization speed. At the lattice defects, tau increases the exchange of tubulin dimers; the above-mentioned changes in tubulin bond strengths are sufficient to explain this effect. In this way, tau accelerates the mobility of defects, driving them to the microtubule end or to mutual annihilation and, thus, contributing to healing lattice defects. MT, microtubule.

https://doi.org/10.1038/s41567-025-03003-7

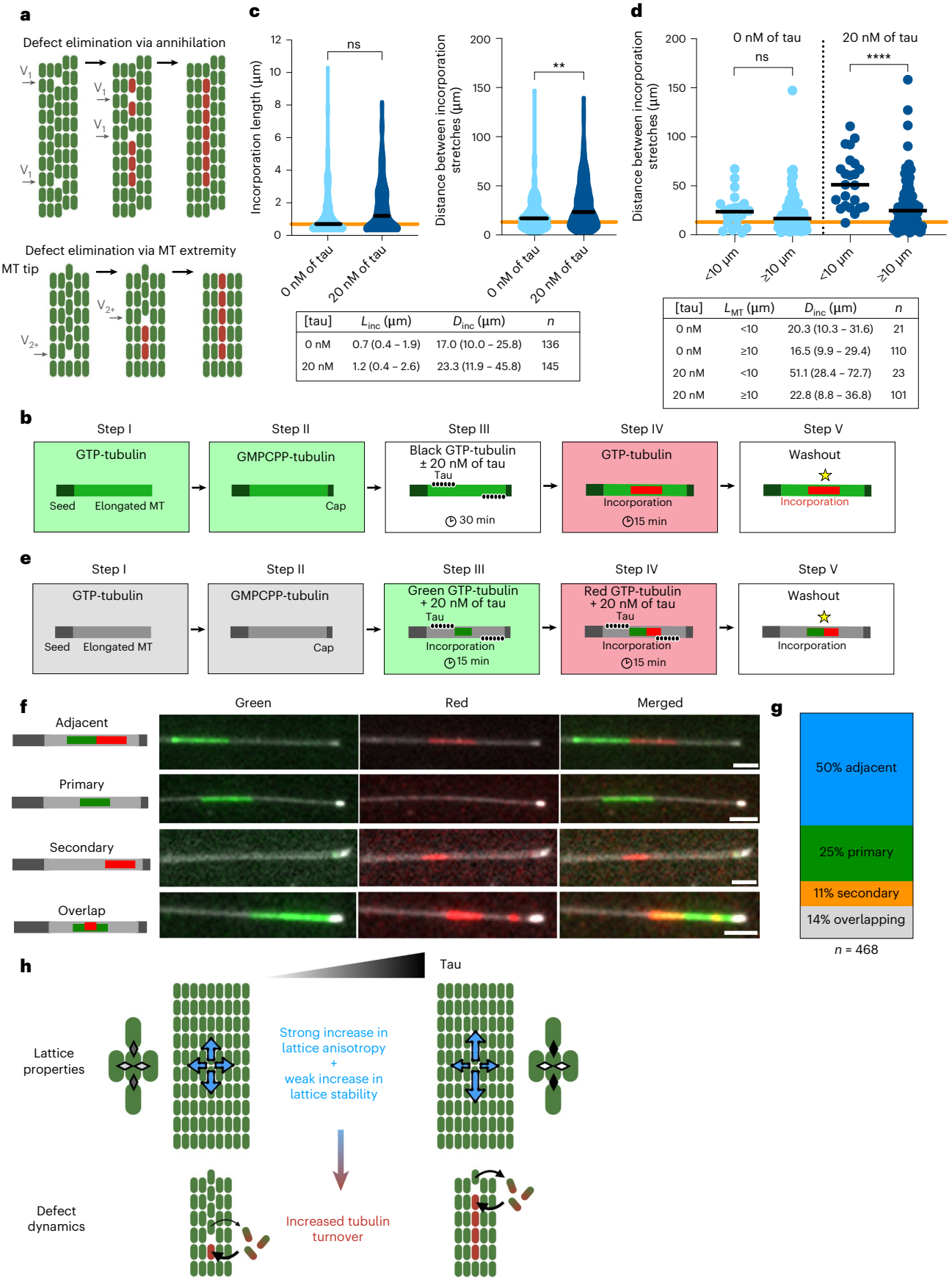

[tau]	L_{inc} (μm)	D_{inc} (μm)	n
0 nM	0.7 (0.4 – 1.9)	17.0 (10.0 – 25.8)	136
20 nM	1.2 (0.4 – 2.6)	23.3 (11.9 – 45.8)	145

[tau]	L_{MT} (μm)	D_{inc} (μm)	n
0 nM	<10	20.3 (10.3 – 31.6)	21
0 nM	≥10	16.5 (9.9 – 29.4)	110
20 nM	<10	51.1 (28.4 – 72.7)	23
20 nM	≥10	22.8 (8.8 – 36.8)	101

Although the origin of this effect is not yet clear, it suggests that tau plays different roles during microtubule polymerization and after microtubule growth. During polymerization, tau may stabilize alternative lattice configurations, whereas after microtubule growth, our observations indicate that tau accelerates the mobility of lattice defects and ultimately facilitates their removal. Once the lattice defects are removed, tau functions as a genuine microtubule stabilizer. Thus, tau acts as a versatile caretaker of the microtubule lattice, capable of promoting dynamic repair processes and maintaining lattice stability.

Our finding that tau, despite being a passive microtubule binder lacking enzymatic activity, facilitates the removal of lattice defects by accelerating tubulin turnover at the defect sites adds to the growing diversity of MAP-mediated interactions with the dynamic microtubule lattice[9]. In contrast to molecular motors, which can actively damage the lattice[11–13], or severing enzymes such as spastin and katanin that amplify such damage[14], tau promotes defect resolution. Other MAPs also respond to lattice discontinuities: CLIP-170 (ref. 5) and CLASP[10], for example, track microtubule plus ends but can also localize to damage sites—probably through the recognition of the transient presence of GTP-tubulin at these sites—and contribute to microtubule stability by promoting rescue and enhancing self-repair. The ability of tau to modulate lattice integrity by increasing defect mobility highlights a distinct, non-enzymatic mode of microtubule regulation. This mechanism may contribute to tau's physiological role in neurons, helping to preserve long-lived, defect-free microtubules that serve as durable tracks for intracellular transport.

Online content

Any methods, additional references, Nature Portfolio reporting summaries, source data, extended data, supplementary information, acknowledgements, peer review information; details of author contributions and competing interests; and statements of data and code availability are available at https://doi.org/10.1038/s41567-025-03003-7.

References

1. Mitchison, T. & Kirschner, M. Dynamic instability of microtubule growth. *Nature* **312**, 237–242 (1984).
2. Schaedel, L. et al. Lattice defects induce microtubule self-renewal. *Nat. Phys.* **15**, 830–838 (2019).
3. Schaedel, L. et al. Microtubules self-repair in response to mechanical stress. *Nat. Mater.* **14**, 1156–1163 (2015).
4. Aumeier, C. et al. Self-repair promotes microtubule rescue. *Nat. Cell Biol.* **18**, 1054–1064 (2016).
5. De Forges, H. et al. Localized mechanical stress promotes microtubule rescue. *Curr. Biol.* **26**, 3399–3406 (2016).
6. Chrétien, D., Metoz, F., Verde, F., Karsenti, E. & Wade, R. Lattice defects in microtubules: protofilament numbers vary within individual microtubules. *J. Cell Biol.* **117**, 1031–1040 (1992).
7. Chrétien, D. & Fuller, S. D. Microtubules switch occasionally into unfavorable configurations during elongation. *J. Mol. Biol.* **298**, 663–676 (2000).
8. Guyomar, C. et al. Changes in seam number and location induce holes within microtubules assembled from porcine brain tubulin and in *Xenopus* egg cytoplasmic extracts. *eLife* **11**, e83021 (2022).
9. Romeiro Motta, M., Biswas, S. & Schaedel, L. Beyond uniformity: exploring the heterogeneous and dynamic nature of the microtubule lattice. *Eur. J. Cell Biol.* **102**, 151370 (2023).
10. Aher, A. et al. CLASP mediates microtubule repair by restricting lattice damage and regulating tubulin incorporation. *Curr. Biol.* **30**, 2175–2183.e6 (2020).
11. Triclin, S. et al. Self-repair protects microtubules from destruction by molecular motors. *Nat. Mater.* **20**, 883–891 (2021).
12. Andreu-Carbó, M., Fernandes, S., Velluz, M.-C., Kruse, K. & Aumeier, C. Motor usage imprints microtubule stability along the shaft. *Dev. Cell* **57**, 5–18.e8 (2022).
13. Budaitis, B. G. et al. A kinesin-1 variant reveals motor-induced microtubule damage in cells. *Curr. Biol.* **32**, 2416–2429.e6 (2022).
14. Vemu, A. et al. Severing enzymes amplify microtubule arrays through lattice GTP-tubulin incorporation. *Science* **361**, eaau1504 (2018).
15. Binder, L. I., Frankfurter, A. & Rebhun, L. I. The distribution of tau in the mammalian central nervous system. *J. Cell Biol.* **101**, 1371–1378 (1985).
16. Peng, I., Binder, L. I. & Black, M. M. Biochemical and immunological analyses of cytoskeletal domains of neurons. *J. Cell Biol.* **102**, 252–262 (1986).
17. Bodakuntla, S., Jijumon, A. S., Villablanca, C., Gonzalez-Billault, C. & Janke, C. Microtubule-associated proteins: structuring the cytoskeleton. *Trends Cell Biol.* **29**, 804–819 (2019).
18. Weingarten, M. D., Lockwood, A. H., Hwo, S. Y. & Kirschner, M. W. A protein factor essential for microtubule assembly. *Proc. Natl Acad. Sci. USA* **72**, 1858–1862 (1975).
19. Drubin, D. G. & Kirschner, M. W. Tau protein function in living cells. *J. Cell Biol.* **103**, 2739–2746 (1986).
20. Drechsel, D. N., Hyman, A. A., Cobb, M. H. & Kirschner, M. W. Modulation of the dynamic instability of tubulin assembly by the microtubule-associated protein tau. *Mol. Biol. Cell* **3**, 1141–1154 (1992).
21. Trinczek, B., Biernat, J., Baumann, K., Mandelkow, E. M. & Mandelkow, E. Domains of tau protein, differential phosphorylation, and dynamic instability of microtubules. *Mol. Biol. Cell* **6**, 1887–1902 (1995).
22. Hernández-Vega, A. et al. Local nucleation of microtubule bundles through tubulin concentration into a condensed tau phase. *Cell Rep.* **20**, 2304–2312 (2017).
23. Prezel, E. et al. Tau can switch microtubule network organizations: from random networks to dynamic and stable bundles. *Mol. Biol. Cell* **29**, 154–165 (2018).
24. Kellogg, E. H. et al. Near-atomic model of microtubule-tau interactions. *Science* **360**, 1242–1246 (2018).
25. McVicker, D. P., Hoeprich, G. J., Thompson, A. R. & Berger, C. L. Tau interconverts between diffusive and stable populations on the microtubule surface in an isoform and lattice specific manner. *Cytoskeleton* **71**, 184–194 (2014).
26. VanBuren, V., Odde, D. J. & Cassimeris, L. Estimates of lateral and longitudinal bond energies within the microtubule lattice. *Proc. Natl Acad. Sci. USA* **99**, 6035–6040 (2002).
27. Sept, D., Baker, N. A. & McCammon, J. A. The physical basis of microtubule structure and stability. *Protein Sci.* **12**, 2257–2261 (2009).
28. Kononova, O. et al. Tubulin bond energies and microtubule biomechanics determined from nanoindentation in silico. *J. Am. Chem. Soc.* **136**, 17036–17045 (2014).
29. Ganser, C. & Uchihashi, T. Microtubule self-healing and defect creation investigated by in-line force measurements during high-speed atomic force microscopy imaging. *Nanoscale* **11**, 125–135 (2019).
30. Wu, Z. et al. Simulations of tubulin sheet polymers as possible structural intermediates in microtubule assembly. *PLoS ONE* **4**, e7291 (2009).
31. Gardner, M. K. et al. Rapid microtubule self-assembly kinetics. *Cell* **146**, 582–592 (2011).
32. LaFrance, B. J. et al. Structural transitions in the GTP cap visualized by cryo-electron microscopy of catalytically inactive microtubules. *Proc. Natl Acad. Sci. USA* **119**, e2114994119 (2022).
33. Katsuki, M., Drummond, D. R. & Cross, R. A. Ectopic A-lattice seams destabilize microtubules. *Nat. Commun.* **5**, 3094 (2014).
34. Kovács, I. & El Sayed, H. Point defects in metals. *J. Mater. Sci.* **11**, 529 (1976).

35. Pertsinidis, A. & Ling, X. S. Diffusion of point defects in two-dimensional colloidal crystals. *Nature* **413**, 147–150 (2001).
36. Mickey, B. & Howard, J. Rigidity of microtubules is increased by stabilizing agents. *J. Cell Biol*. **130**, 909–917 (1995).
37. Felgner, H., Frank, R. & Schliwa, M. Flexural rigidity of microtubules measured with the use of optical tweezers. *J. Cell Sci*. **109**, 509–516 (1996).
38. Felgner, H. et al. Domains of neuronal microtubule-associated proteins and flexural rigidity of microtubules. *J. Cell Biol*. **138**, 1067–1075 (1997).
39. Schaap, I. A. T., Hoffmann, B., Carrasco, C., Merkel, R. & Schmidt, C. F. Tau protein binding forms a 1 nm thick layer along protofilaments without affecting the radial elasticity of microtubules. *J. Struct. Biol*. **158**, 282–292 (2007).
40. Nishida, K. et al. Effects of three microtubule-associated proteins (MAP2, MAP4, and tau) on microtubules' physical properties and neurite morphology. *Sci. Rep*. **13**, 8870 (2023).

Methods

Molecular cloning, expression and purification of tau

The gene coding for Tau2N4R was amplified by polymerase chain reaction using the primers flanked with the restriction sites NotI and AscI at the 5′ (AATAATAACATGCGGCCGCAA TGGCTGAGCCCCGCC) and 3′ (AATAATAACATGGCGCGCCCAAACCCTGCTTGGCCAG) ends, respectively. The resulting product was inserted in the FlexiBac[41] vector backbone with either C-terminal monoGFP followed by 3C protease cleavage site and 6×Histidine tag or without the fluorescent monoGFP tag. The construct sequences were then confirmed by digestion and sequencing. Plasmid vectors with the tau2n4r gene was then co-transfected with a replication-defective bacmid DNA into Sf9 cells. Homologous recombination between flanking sequences in both piece of DNA introduces the gene of interest into the viral genome and rescues viral replication and subsequent amplification in Sf9 insect cells. For protein expression, SF9 cells were infected with recombinant passage 2 viruses with a ratio of 1:100 (v/v) and harvested 72 h post-infection by centrifugation at 500*g* for 10 min. The harvested cells were resuspended in the lysis buffer (25 mM of HEPES, 150 mM of KCl, 5% glycerol, 0.1% Tween 20 (v/v), 20 mM of imidazole, 1 mM of TCEP and 1× protease inhibitor cocktail (cocktail III Merck calbiochem, 535140)). Cells were then lysed using Emulsiflex-C5 (Avestin). All further steps were then performed at 4 °C or under ice. The lysate was then spun at 186,000*g* for 45 min. The supernatant was filtered through a 0.45-µm syringe filter and passed through a 1-ml His-trap column (29051021, Cytiva) pre-equilibrated with ten-column volume of equilibration buffer (50 mM of HEPES, 300 mM of KCl, 5% glycerol, 0.2% Tween 20 (v/v), 20 mM of imidazole, 1 mM of TCEP, pH 7.2). The protein was then eluted by passing the elution buffer (equilibration buffer supplemented with 200 mM of imidazole). The 6×Histidine tag was then removed by incubating the eluted fractions with PreScission protease (3C HRV protease, 1:100, 1 µg of enzyme per 100 µg of protein, overnight at 4 °C). Protease-treated protein fractions were then concentrated using Amicon spin filters (molecular weight cut-off, 30 kDa) with buffer exchanged to equilibration buffer. The protein of interest was further purified by size exclusion chromatography using Superdex 200 Increase (28990944, Cytiva) column with an ÄKTA Pure chromatography system (GE Healthcare) in a storage buffer (25 mM of HEPES, 150 mM of KCl, 5% glycerol, 0.1% Tween 20 (v/v), 1 mM of TCEP, pH 7.2). Collected peak fractions were concentrated using Amicon Ultra 30K (Millipore), aliquoted and then snap-frozen in liquid nitrogen and stored at −80 °C. Sodium dodecyl sulfate–polyacrylamide gel electrophoresis was used to determine the purity of isolated proteins and for protein concentration estimation by running serial dilutions of BSA (1 mg ml^{-1}) alongside appropriate dilutions of the proteins on a 4%–12% BisTris sodium dodecyl sulfate–polyacrylamide gel electrophoresis precast gel in MOPS buffer (Life Technologies), stained with Coomassie for 60 min and destained in distilled water. Stained gels were imaged in an imaging station (c300, Azure Biosystems). The integrated intensity of the protein bands of interest was quantified using the 'Gels' tool in Fiji[42]. Linear fitting of the integrated intensity versus concentration of BSA provided a calibration curve, which was then used to estimate the concentration of desired proteins.

Tubulin purification and labelling

Tubulin was purified from fresh bovine brain by three cycles of temperature-dependent assembly and disassembly in Brinkley Buffer 80 (BRB80 buffer; BRB buffer: 80 mM of PIPES, pH 6.8, 1 mM of EGTA and 1 mM of $MgCl_2$ plus 1 mM of GTP). MAP-free neurotubulin was purified by using low- and high-salt buffer (high-molarity PIPES buffer) in 1 M of PIPES, pH 6.9, supplemented with KOH, 10 mM of $MgCl_2$, 20 mM of EGTA and subsequent cation-exchange chromatography (EMD SO, 650 M, Merck) in 50 mM of PIPES, pH 6.8, supplemented with 1 mM of $MgCl_2$ and 1 mM of EGTA. Purified tubulin was obtained after, in total, three cycles of polymerization and depolymerization. Fluorescent tubulin (ATTO-488- and ATTO-565-labelled tubulin) and biotinylated tubulin were prepared as previously described[43]: microtubules from neurotubulin were polymerized at 37 °C for 30 min and layered onto cushions of 0.1-M NaHEPES, pH 8.6, 1-mM $MgCl_2$, 1-mM EGTA and 60% v/v glycerol, and sedimented by high centrifugation at 37 °C. Then, the microtubules were resuspended in 0.1 M of NaHEPES, pH 8.6, 1 mM of $MgCl_2$, 1 mM of EGTA and 40% v/v glycerol, and labelled by adding 1/10 volume of 100-mM NHS-ATTO (ATTO Tec) or NHS-LC-LC-biotin (EZ-link, Thermo) for 10 min at 37 °C. The labelling reaction was stopped using two volumes of 2× BRB80, containing 100 mM of potassium glutamate and 40% v/v glycerol, and then the microtubules were sedimented onto cushions of BRB80 supplemented with 60% glycerol. Microtubules were resuspended in BRB80, and an additional cycle of polymerization and depolymerization was performed before use.

Cover-glass treatment

The micropatterning technique was adapted from ref. 44. Cover glasses were cleaned by successive chemical treatments: 30 min in acetone, 15 min in ethanol (96%), rinsing in ultrapure water, 2 h in Hellmanex III (2% in water, Hellmanex) and rinsing in ultrapure water. Cover glasses were air dried and incubated for 3 days in a solution of tri-ethoxysilane-PEG (30 kDa, Creative PEGWorks) or a 1:10 mix of tri-ethoxy-silane-PEG-biotin and tri-ethoxy-silane-PEG at 1 mg ml^{-1} in 96% ethanol and 0.1% HCl, with gentle agitation at room temperature. Cover glasses were then successively washed in ethanol and ultrapure water, air dried and stored at 4 °C.

Microtubule growth, capping and tubulin incorporation

Microtubule seeds were prepared at 10-µM tubulin concentration (30% ATTO-488-labelled or ATTO-565-labelled tubulin and 70% biotinylated tubulin) in BRB80 supplemented with 0.5 mM of GMPcPP at 37 °C for 1 h. The seeds were incubated with 50 µM of paclitaxel (Merck) at room temperature for 30 min and then sedimented at 156,000*g* at 25 °C and resuspended in BRB80 supplemented with 0.5 mM of GMPcPP and 50 µM of paclitaxel. Seeds were stored in liquid nitrogen and quickly warmed to 37 °C before use.

A flow-cell chamber with an approximate volume of 40 µl with an entry and exit site was constructed with double-sided adhesive tape with a glass coverslip functionalized and passivated with SiPEG (top) or SiPEG and SiPEG-Biotin (9:1, bottom). The flow chamber was perfused for 30 s with neutravidin (50 µg ml^{-1} in 1× BRB80; Fisher Scientific), passivated for 30 s with PLL-*g*-PEG (Pll 20 K-G35-PEG2K, Jenkam Technology) at 0.1 mg ml^{-1} in 10 mM of NaHEPES (pH 7.4) and washed again with 1× BRB80. Microtubule seeds were flushed into the chamber at a high flow rate to ensure the parallel orientation of seeds to the flow direction. Non-attached seeds were washed out immediately using BRB80 supplemented with 1 mg ml^{-1} of casein.

Seeds were elongated with a mix containing 11 µM of tubulin (5% to 20% labelled, green fluorescent) in 0.7× BRB80 and 0.38× MAP buffer (500 mM of phosphate buffer, 1 M of KCl, 10 mM of DTT, pH 7.9) supplemented with 1 mM of GTP, an oxygen scavenger cocktail (22 mM of DTT, 1.2 mg ml^{-1} of glucose, 8 µg ml^{-1} of catalase and 40 µg ml^{-1} of glucose oxidase), 1 mg ml^{-1} of casein and 0.033% (w/v) methyl cellulose (1,500 cP, Sigma) at 37 °C. GMPcPP caps were grown by substituting in the afore-mentioned buffer GTP with 0.5 mM of GMPcPP (Jena Bioscience) and using 3 µM of tubulin (100% fluorescently labelled) at 37 °C. Capping extends the microtubule lifetime and allows for the examination of lattice turnover over a period of several minutes despite the dynamic instability in vitro. For incorporation experiments, the same buffer as for seed elongation was used, supplemented with 8 µM of tubulin (100% fluorescently labelled) along with 0 nM, 0.5 nM or 20 nM of 2N4R-GFP tau or unlabelled 2N4R tau diluted in 1× BRB80. Microtubules were incubated in this buffer for 15 min or 30 min at 37 °C before replacing it with a washing buffer (with the same buffer as that for seed elongation with 50 µM of paclitaxel and without free tubulin)

for imaging. For fracture experiments, a buffer containing the same supplements but without Taxol and free tubulin was used. For tubulin incorporation along with fracture experiments, the first incorporation was performed as mentioned above both in the presence and absence of tau and subsequently imaged microtubules in tubulin-free buffer until fracture, as discussed earlier. In Extended Data Fig. 3, unlabelled tubulin was used for microtubule elongation and the microtubules were imaged by combining interference reflection microscopy with epifluorescence microscopy. For the tubulin incorporation experiments after a 5-min washout phase (Fig. 4e–h), only those microtubules that were aligned with the flow direction were analysed to minimize flow-induced damage of the microtubules already weakened by the preceding tubulin loss. Particular care was taken that the flow was applied as gently as possible to further reduce potential flow-induced damage. Visual inspection of the sample before and after flow was used to confirm that the microtubules had not fractured.

Imaging and image analysis

Microtubules were visualized using a point scanning confocal microscope (ZEISS LSM 900) with Airyscan 2 and Axiocam 705 camera. The microscope stage was maintained at 37 °C through a cage incubator (PECON). Time-lapse images were recorded using ZenBlue software (v. 3.2).

Microtubule fracture experiments were performed and visualized on an objective-based orbital total internal reflection fluorescence microscope (Nikon Eclipse Ti2, modified by ViSitron Systems) and an electron-multiplying charge-coupled device camera (Andor iXon Life) at minimal laser intensity. The microscope stage was maintained at 37 °C using a warm stage controller (OkoLabs). Time-lapse recording was performed using VisiView software (v. 6.0).

To visualize incorporation, images were typically taken every 0.5 s, and five images were overlaid and averaged. Line scans of the red fluorescence intensity along the microtubule (Fig. 1c) were used to identify the stretches of incorporated tubulin. Stretches of tubulin incorporation were identified as corresponding to zones of fluorescent intensities that were at least 2.5 times above the background. Incorporation lengths were measured using the full-width at half-maximum of the intensity profiles; only incorporation stretches of at least 300-nm length were taken into account, based on the resolution limit of the microscope. For fracture experiments, images were taken every 5 s. Videos were processed to improve the signal-to-noise and signal-to-background ratios (smooth and subtract background functions of ImageJ (v. 1.54j)). Lengths of damaged regions were determined by line scans along the microtubules in the frame just before fracture; regions corresponding to a drop of at least 50% of the fluorescence intensity of the intact lattice were considered damaged.

Quantification of the number of incorporated dimers in incorporation stretches

To estimate the loss of lattice fluorescence at incorporation stretches (normalized lattice fluorescence; Fig. 2f, bottom), we averaged the green fluorescence signal over the length of an incorporation stretch and divided it by the averaged lattice fluorescence outside of the incorporation stretch on the same microtubule (Fig. 2f, top). We performed this analysis for ten frames per incorporation stretch and averaged the values. To estimate the lateral extent of tubulin incorporation (normalized incorporation fluorescence; Fig. 2g (bottom) and Fig. 4h), we took the images from our incorporation experiments in which we occasionally observed microtubule growth beyond the cap with 100% red-labelled tubulin and used it as the reference stretch (Fig. 2g, top). We then divided the averaged red fluorescence intensity per length of an incorporation stretch by the reference intensity per length measured at the cap. We performed this analysis for ten frames per incorporation stretch and averaged the values.

Single-molecule photobleaching experiments and analysis

Tau proteins were diluted in cold 1× BRB80 to a concentration of a few tenths of a micromole and centrifuged to remove aggregates (10 min/4 °C/215,000*g* in Type 70 Ti rotor (Beckman)). Before use, tau proteins were further serial diluted to a final concentration of 50 pM. In the flow chamber, 50 µl of the diluted 2N4R-GFP tau was perfused for 5 min at room temperature. The chamber was then washed three times with 100 µl of 1× BRB80 to remove unbound proteins and then sealed with Valap. Images were recorded in the continuous streaming mode for 2 min with 300-ms exposure time and high laser power to photobleach the isolated molecules.

For analysis, a region of interest with uniform illumination was selected, and the stack was cropped. The fluorescence intensity fluctuations over time of each fluorescent tau molecule were obtained using the Stowers Institute ImageJ plug-in (Extended Data Fig. 1).

Single-molecule total internal reflection fluorescence microscopy

An objective-based orbital total internal reflection fluorescence microscope with single-fluorophore sensitivity was used for the detection of fluorescently labelled microtubules and tau molecules. Seeds were elongated with a mix containing 11 µM of tubulin (20% labelled with ATTO-565) in 0.7× BRB80 and 0.38× MAP Buffer (500 mM of phosphate buffer, 1 M of KCl, 10 mM of DTT, pH 7.9) supplemented with 1 mM of GTP, an oxygen scavenger cocktail (22 mM of DTT, 1.2 mg ml^{-1} of glucose, 8 µg ml^{-1} of catalase and 40 µg ml^{-1} of glucose oxidase), 1 mg ml^{-1} of casein and 0.033% (w/v) methyl cellulose (1,500 cP, Sigma) at 37 °C. GMPcPP caps were grown by substituting in the aforementioned buffer GTP with 0.5 mM of GMPcPP (Jena Bioscience) and using 3 µM of tubulin (100% labelled with ATTO-565) at 37 °C. The assay buffer was supplemented with a total of 20-nM 2N4R tau of which 50 pM was labelled with GFP and free tubulin along with the same oxygen scavenger system as mentioned above to minimize the bleaching of fluorophores. Additionally, a time-lapse video for 100 frames was recorded using the same laser power and same exposure obtained during the single-molecule photobleaching experiment. For kymograph reconstruction, each sample video of the motion of tau along the microtubules was converted to successive stacks and eventually to a three-dimensional array of greyscale data. This data array was then converted into a binary array using an intensity threshold. The islands in this space–time configuration were identified by the Hoshen–Kopelman cluster detection algorithm. To eliminate background noise, small islands were identified and removed by applying a minimum-island-size threshold. Each of the remaining islands represented a kymograph. The duration of diffusion and the scanned distance by tau along the microtubule for each kymograph were obtained by measuring the extent of the corresponding island along the time and space coordinates. The diffusion coefficient for each kymograph was calculated using the corresponding duration and scanned distance. The probability distributions of the duration of diffusion and the diffusion coefficient were found to be well fitted by an exponential and a Gaussian function, respectively. To calculate the mean fraction of tau-covered microtubule lattice, we assumed that each bound tau molecule connects five tubulin dimers.

Statistical methods

All statistical analyses were performed using GraphPad Prism 9.5. The confocal-microscopy-observed microtubule incorporation patterns were examined by concatenating all microtubules in random order and determining the centre-to-centre distance between two adjacent incorporation locations. To test the significance between incorporation lengths and distances between incorporation distributions obtained for the various conditions as well as for the lengths of the damaged regions and number of incorporated protofilaments, we used the Mann–Whitney (two-tailed) test as a non-parametric alternative to a *t*-test, given that the distributions are non-Gaussian. To analyse the differences in the normalized lattice

fluorescence, we used an unpaired *t*-test, given that the distributions appear Gaussian and with similar variances. Microtubule lifetime was quantified by manually counting the microtubule number at each frame within several fields of view, for 50 min. We used the Mantel–Cox log-rank test to assess differences in microtubule survival curves.

CG MD simulations

To estimate the free energy associated with tubulin dissociation in the presence and absence of tau, we performed CG MD simulations. The atomistic starting structure of tau, spanning three tubulin monomers (1 αβ-tubulin hetero-dimer, 1 β-tubulin monomer), was obtained from the Protein Data Bank (PDB ID: 6CVN[24]). The atomistic structure was converted to a CG representation using the Martinize script[45] and modelled with the Martini-3 force field[46]. The structure of the monomers was preserved using an elastic network between the backbone beads (force constant, 700 kJ mol^{-1} nm^{-2}). The CG tau–tubulin complex was placed in a simulation box with dimensions of 20 nm × 20 nm × 20 nm, such that the microtubule would be oriented along the *z* axis. The box was solvated with 62,508 standard Martini water beads and neutralized by adding 50 Na^+ ions. The system was energy minimized using the steepest-descent algorithm. During equilibration, Lennard–Jones and Coulomb interactions were treated with a cut-off of 1.1 nm. The temperature was maintained at 310 K using velocity rescaling[47] with a coupling constant of 0.1 ps, whereas the pressure was maintained at 1 bar using an isotropic Berendsen barostat[48] with a coupling constant of 6 ps. Bonds were constrained using the LINCS algorithm[49]. Equilibration was performed for 20 ns with the GROMACS 2021.1 simulation package[50], with position restraints applied only on tau.

The final structure from the equilibration was used to generate starting configurations for US simulations. The reaction coordinate was defined as the centre-of-mass distance between adjacent monomers. A monomer was pulled away by 3 nm over 200 ns using an umbrella potential, where pull forces were applied only along the *z* direction. A pull rate of 1.5×10^{-5} nm ps^{-1} and a force constant of 100,000 kJ mol^{-1} nm^{-2} were applied. During pulling and US simulations, we applied position-restraint potentials to avoid rotations of the overall monomer and to avoid the drifting of monomers in the *x*–*y* plane, because such motions could lead to sampling problems. Accordingly, except for the interface residues of the adjacent tubulin monomers that were fully flexible (residues 130–133, 163, 199, 241–265, 321–337 and 345–355 of monomer 2 and residues 70–78, 95–102, 175–183, 206–224 and 393–413 of monomer 3), position restraints were applied in the *x* and *y* directions on the backbone beads of all other residues with a force constant of 500 kJ mol^{-1} nm^{-2}. No restraints were applied to the tau residues interacting with the pulled monomer 3, whereas the rest of the tau residues had backbone position restraints with a force constant of 500 kJ mol^{-1} nm^{-2}, thereby restraining the interfaces of tau with monomers 1 and 2. All other simulation parameters were identical with those used during equilibration.

From the pulling simulations, 170 structures were extracted for US simulations. The US windows were spaced at 0.015 nm with a force constant of 10,000 kJ mol^{-1} nm^{-2} up to a distance of approximately 1.05 nm between the adjacent monomers. At larger distances, the spacing was set to 0.02 nm with a force constant of 5,000 kJ mol^{-1} nm^{-2}. Each US window was simulated for 100 ns using GROMACS 2021.1 (ref. 51) with a time step of 20 fs. The potential of the mean force was calculated after skipping the first 40 ns of each window for equilibration with the weighted histogram analysis method implementation gmx wham of GROMACS 2021.1 (refs. 51,52). Statistical errors were estimated using 50 rounds of bootstrapping of complete histograms. The potential of mean force for the system without tau followed the same protocol, except that tau was removed from the equilibrated structure.

Reporting summary

Further information on research design is available in the Nature Portfolio Reporting Summary linked to this article.

Data availability

All data needed to evaluate the conclusions in the paper are present in the Article and its Supplementary Information. The data that support the plots within this paper and other findings of this study are available via Zenodo at https://doi.org/10.5281/zenodo.13950636 (ref. 53).

Code availability

Code used to produce the simulations in the paper is available via Zenodo at https://doi.org/10.5281/zenodo.13950636 (ref. 53).

References

41. Lemaitre, R. P., Bogdanova, A., Borgonovo, B., Woodruff, J. B. & Drechsel, D. N. FlexiBAC: a versatile, open-source baculovirus vector system for protein expression, secretion, and proteolytic processing. *BMC Biotechnol.* **19**, 20 (2019).
42. Schindelin, J. et al. Fiji: an open-source platform for biological-image analysis. *Nat. Methods* **9**, 676–682 (2012).
43. Hyman, A. et al. Preparation of modified tubulins. *Methods Enzymol.* **196**, 478–485 (1991).
44. Portran, D., Gaillard, J., Vantard, M. & Thery, M. Quantification of MAP and molecular motor activities on geometrically controlled microtubule networks. *Cytoskeleton* **70**, 12–23 (2013).
45. De Jong, D. H. et al. Improved parameters for the martini coarse-grained protein force field. *J. Chem. Theory Comput.* **9**, 687–697 (2013).
46. Souza, P. C. T. et al. Martini 3: a general purpose force field for coarse-grained molecular dynamics. *Nat. Methods* **18**, 382–388 (2021).
47. Bussi, G., Donadio, D. & Parrinello, M. Canonical sampling through velocity rescaling. *J. Chem. Phys.* **126**, 014101 (2007).
48. Berendsen, H. J. C., Postma, J. P. M., Van Gunsteren, W. F., DiNola, A. & Haak, J. R. Molecular dynamics with coupling to an external bath. *J. Chem. Phys.* **81**, 3684–3690 (1984).
49. Hess, B., Bekker, H., Berendsen, H. J. C. & Fraaije, J. G. E. M. LINCS: a linear constraint solver for molecular simulations. *J. Comput. Chem.* **18**, 1463–1472 (1997).
50. Abraham, M. J. et al. GROMACS: high performance molecular simulations through multi-level parallelism from laptops to supercomputers. *SoftwareX* **1–2**, 19–25 (2015).
51. Hub, J. S., De Groot, B. L. & Van Der Spoel, D. g_wham—a free weighted histogram analysis implementation including robust error and autocorrelation estimates. *J. Chem. Theory Comput.* **6**, 3713–3720 (2010).
52. Kumar, S., Rosenberg, J. M., Bouzida, D., Swendsen, R. H. & Kollman, P. A. The weighted histogram analysis method for free-energy calculations on biomolecules. I. The method. *J. Comput. Chem.* **13**, 1011–1021 (1992).
53. Biswas, S. et al. Tau accelerates tubulin exchange in the microtubule lattice. *Zenodo* https://doi.org/10.5281/zenodo.13950636 (2025).

Acknowledgements

S.B. and L.S. were supported by the Deutsche Forschungsgemeinschaft (DFG, German Research Foundation; grant number SFB 1027/A13) and through Saarland University's NanoBioMed Young Investigator Grant awarded to L.S. R.G., C.R. and S.D. were supported by DFG grant number SFB 1027/A8 and the TUD Dresden University of Technology. C.S.P. and J.S.H. were supported by DFG grant numbers SFB 1027/B7 and INST 256/539-1. R.S. acknowledges support through DFG grant number SFB 1027/A7. K.J. and A.Z. were supported through the Idex Université Grenoble-Alpes. The numerical computations by A.Z. and K.J. were performed using the Cactus cluster of the CIMENT infrastructure, which was supported by the Rhône-Alpes region. We are grateful to P. Beys, who manages the cluster.

Author contributions

L.S., K.J. and S.D. conceived and guided the project. L.S., S.D., S.B., S.N., M.G., R.G. and C.R. designed the experiments. S.B. carried out the experiments. M.G. purified the tubulin. R.G. and C.R. provided tau and related expertise. A.Z. and K.J. designed and carried out the kinetic Monte Carlo simulations. J.S.H. and C.S.P. designed and carried out the MD simulations. R.S. analysed the single-molecule experiments. L.S., S.D. and K.J. wrote the manuscript. All authors provided critical feedback and helped to shape the research and analysis.

Funding

Open access funding provided by Universität des Saarlandes.

Competing interests

The authors declare no competing interests.

Additional information

Extended data is available for this paper at https://doi.org/10.1038/s41567-025-03003-7.

Supplementary information The online version contains supplementary material available at https://doi.org/10.1038/s41567-025-03003-7.

Correspondence and requests for materials should be addressed to Karin John or Laura Schaedel.

Peer review information *Nature Physics* thanks Xiao-Han Li and the other, anonymous, reviewer(s) for their contribution to the peer review of this work.

https://doi.org/10.1038/s41567-025-03003-7

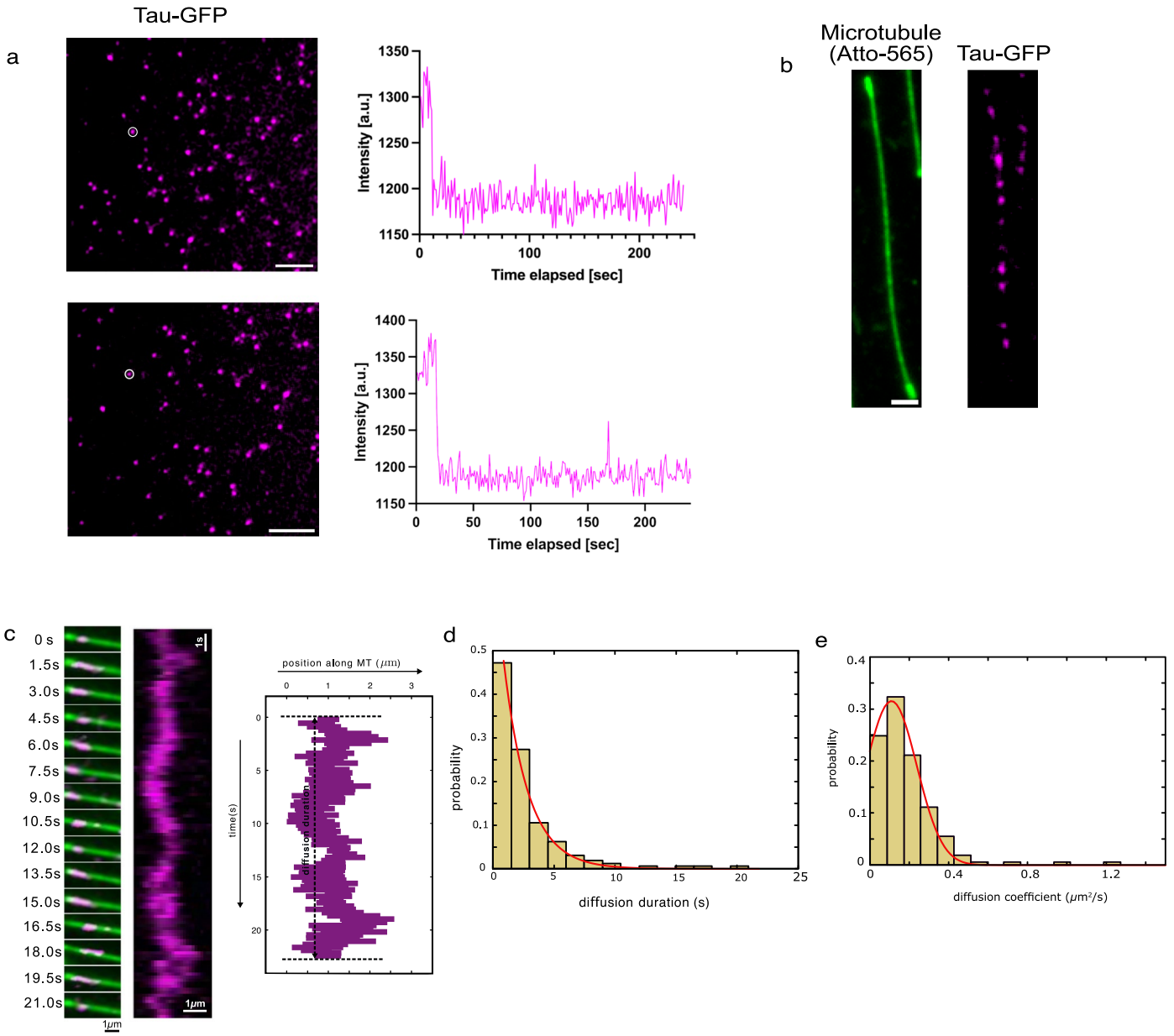

Extended Data Fig. 1 | Diffusive motion and dynamic binding/unbinding of single tau molecules on the microtubule lattice. a. Example images for single-molecule photobleaching. 50 pM surface-attached Tau-GFP were exposed for 300 ms. The fluorescence intensity profiles correspond to the highlighted. areas. One-step bleaching indicates the presence of monomeric tau. Scale bars: 5 µm. **b**. Example image of a microtubule (Atto-565-labeled) with 20 nM unlabeled tau and 50 pM GFP-labeled tau. The mean fraction of tau-covered microtubule lattice is 0.191±0.008. Scale bar: 3 µm. **c**. Left: Sequential frames of a tau molecule (GFP-labeled, shown in magenta) moving along a microtubule (Atto-565-labeled, shown in green). The time intervals are indicated. Center: The corresponding kymograph of the movement of tau shown in the left panel. Right: The reconstructed kymograph. **d**. Probability distribution of the duration of diffusion of tau along microtubules. The mean duration of diffusion is 3.7±0.7 s. The line represents an exponential tail fit. **e**. Probability distribution of the diffusion coefficient of tau along microtubules. The mean diffusion coefficient is 0.21±0.03 µm^2/s. The line represents a Gaussian fit. Given tau's rapid dynamics (short dwell time (**d**) and fast diffusion (**e**)) compared to the slow time scale of lattice turnover, we can model its effect on the lattice using an effective approach (details in the model description in the SI).

https://doi.org/10.1038/s41567-025-03003-7

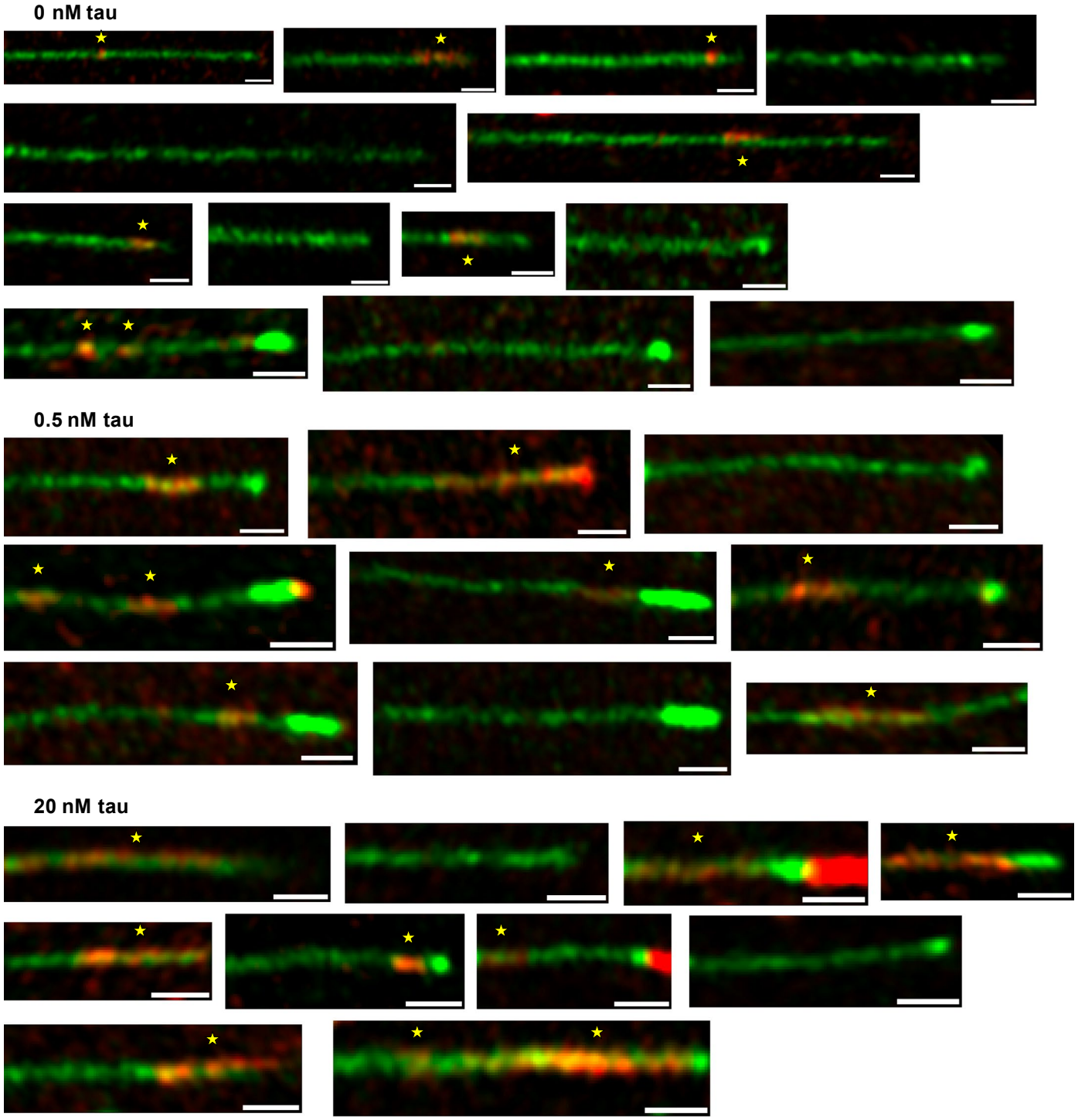

Extended Data Fig. 2 | Example images of tubulin incorporation. Example images of tubulin incorporation (red) along the microtubule lattice (green) at 15 min for 0 nM, 0.5 nM and 20 nM tau (related to Fig. 1). Incorporation spots are marked with a star. Scale bars: 1 µm.

https://doi.org/10.1038/s41567-025-03003-7

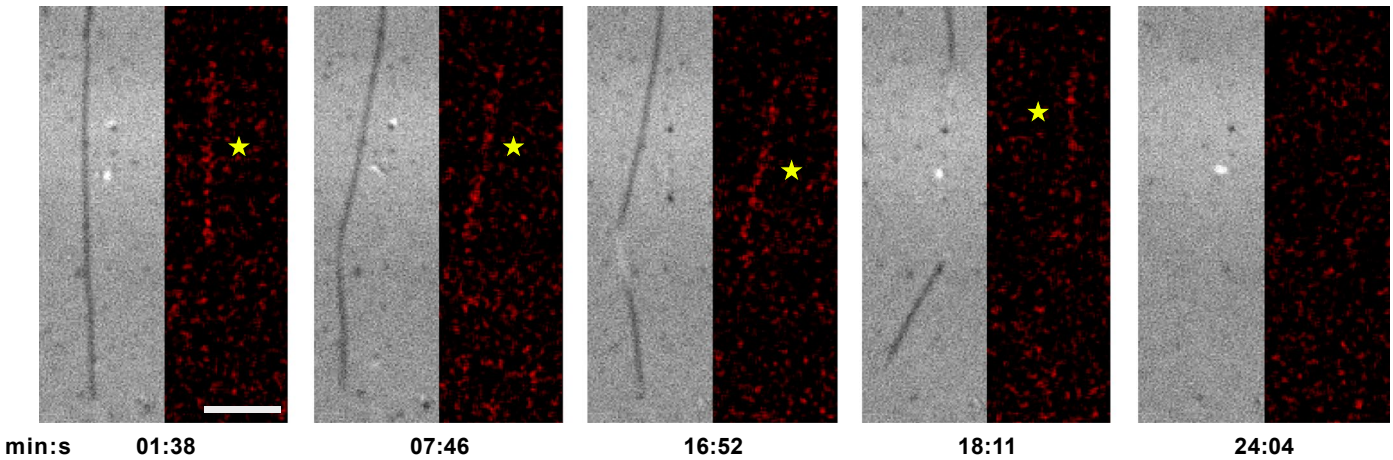

Extended Data Fig. 3 | Microtubule fracture events investigated on unlabeled microtubules. Label-free microtubules were used for fracture experiments to exclude a possible influence of the fluorescent label or the interface between red/green labels on the fracture behavior. The image sequence shows interference reflection microscopy (left) / epifluorescence (right) images of microtubule fracture in the absence of free tubulin after a 15 min incorporation step with Atto-488-labeled tubulin (shown in red, the star marks the incorporation stretch) in the presence of 20 nM tau. Scale bar: 3 µm.

https://doi.org/10.1038/s41567-025-03003-7

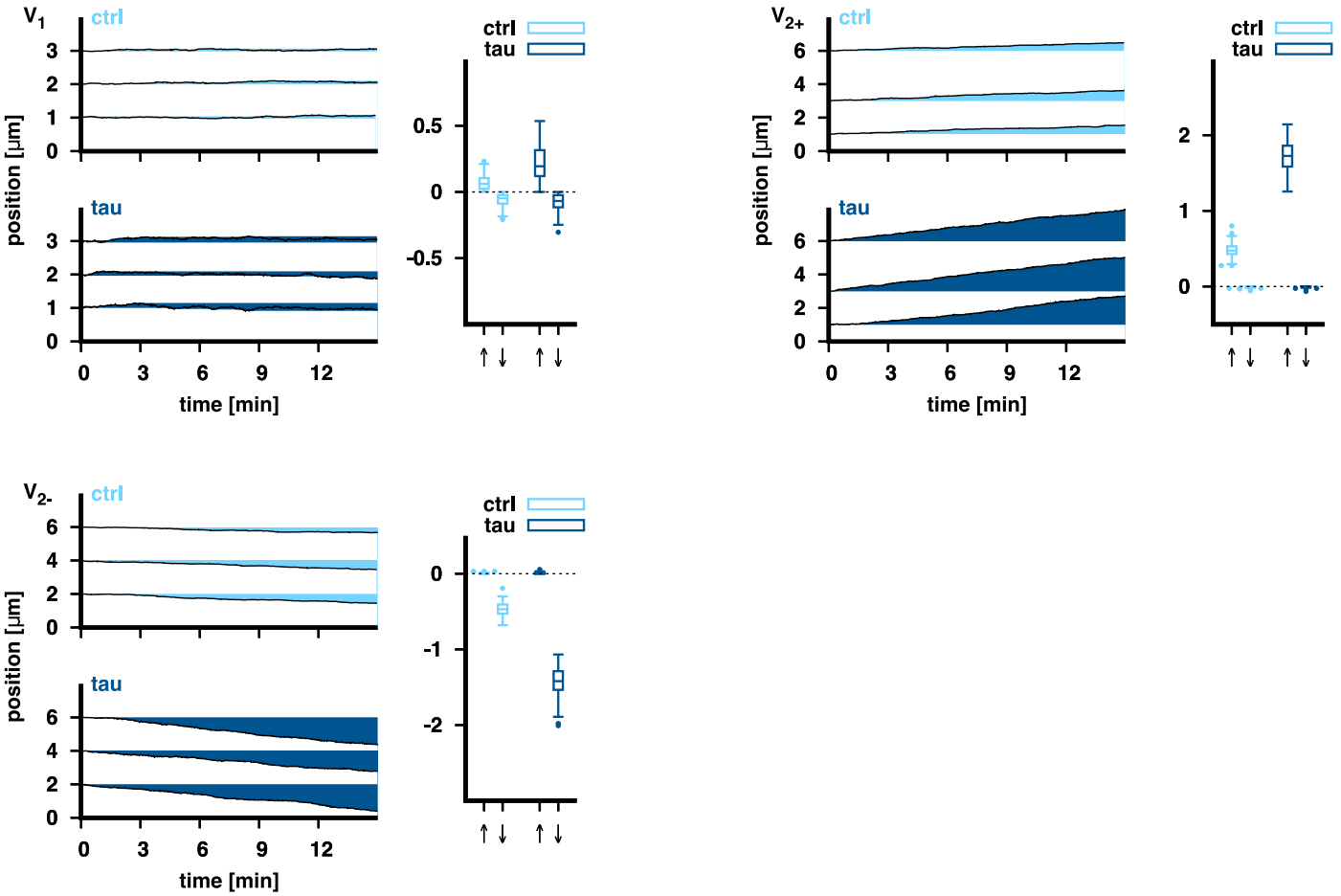

Extended Data Fig. 4 | Simulation of tubulin incorporation at defects. Example trajectories (left panels) for V_1, V_{2+}, V_{2-} defects (as indicated in the left top corner of each plot) in the absence (ctrl, light blue color) and in the presence of tau (tau, dark blue color). The right panel shows the maximum and minimum positions where free tubulin was incorporated. The position of the defect at time zero is at zero. Horizontal lines and boxes indicate the medians and IQRs. Whiskers extend to the most distant point whose value lies within 1.5 times of the IQR. Points lying outside the whiskers are drawn individually. n = 100 for each defect type and condition. An asymmetry of maximum and minimum positions w.r.t. zero indicates that the defect motion has a ballistic component. Parameters are $\Delta G_S = 0.5$ kT, and $\Delta G_{tot} = -36$ kT, $A = 1.5$ (control) and $\Delta G_{tot} = -36.2$ kT, $A = 2.1$ (tau) with $\Delta G_V = 1.25$ kT and as indicated in Supplementary Table 2 in the SI.

https://doi.org/10.1038/s41567-025-03003-7

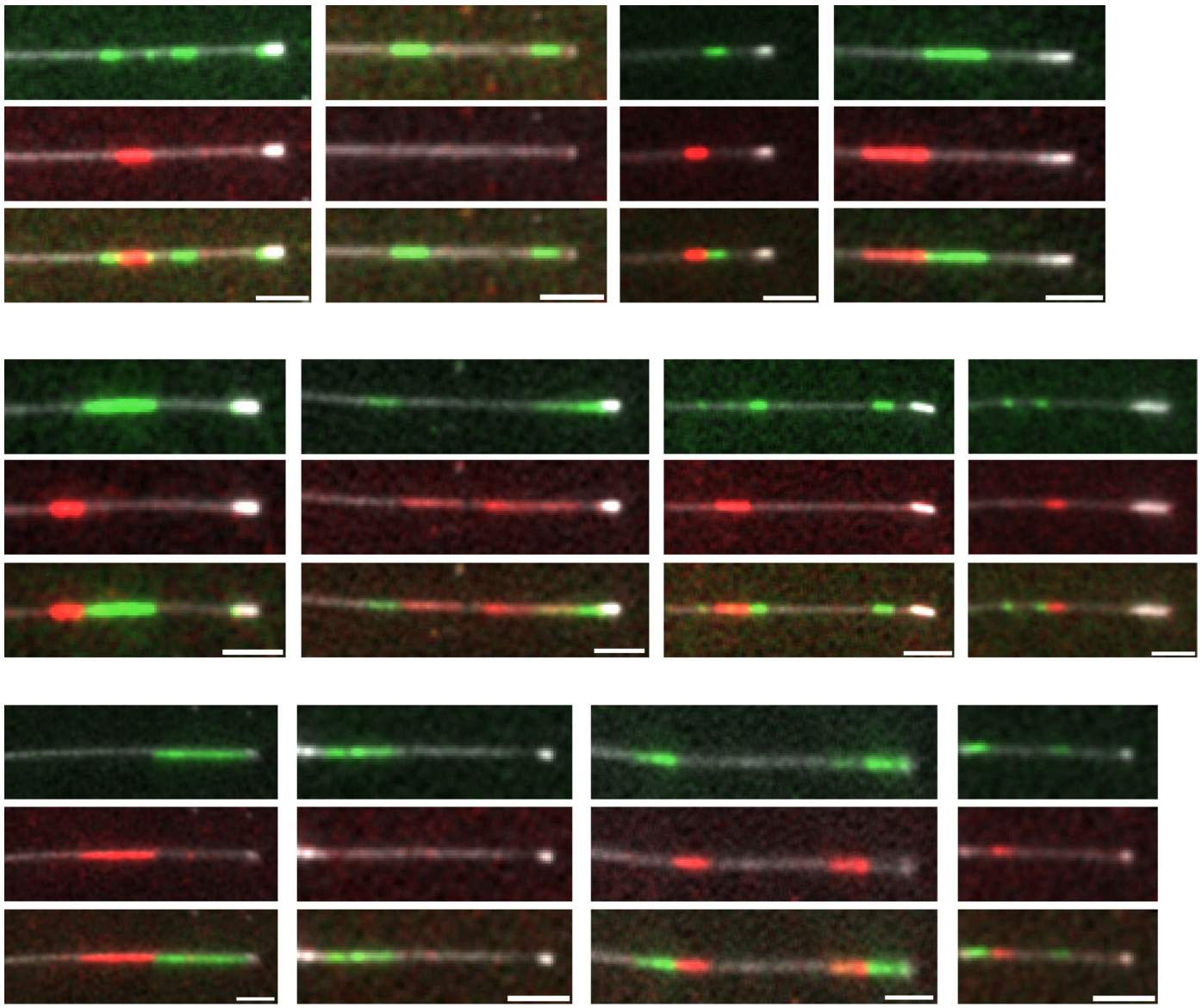

Extended Data Fig. 5 | Tubulin incorporation is caused by defect mobility. Example images of microtubules (far-red labeled, shown in grey) showing two-color tubulin incorporation stretches (corresponding to Fig. 6e–g). Scale bars: 5 µm.

nature portfolio

Corresponding author(s): Laura Schaedel, Karin John

Last updated by author(s): Jul 8, 2025

Reporting Summary

Nature Portfolio wishes to improve the reproducibility of the work that we publish. This form provides structure for consistency and transparency in reporting. For further information on Nature Portfolio policies, see our Editorial Policies and the Editorial Policy Checklist.

Statistics

For all statistical analyses, confirm that the following items are present in the figure legend, table legend, main text, or Methods section.

n/a	Confirmed	
☐	☒	The exact sample size (*n*) for each experimental group/condition, given as a discrete number and unit of measurement
☐	☒	A statement on whether measurements were taken from distinct samples or whether the same sample was measured repeatedly
☐	☒	The statistical test(s) used AND whether they are one- or two-sided *Only common tests should be described solely by name; describe more complex techniques in the Methods section.*
☒	☐	A description of all covariates tested
☐	☒	A description of any assumptions or corrections, such as tests of normality and adjustment for multiple comparisons
☐	☒	A full description of the statistical parameters including central tendency (e.g. means) or other basic estimates (e.g. regression coefficient) AND variation (e.g. standard deviation) or associated estimates of uncertainty (e.g. confidence intervals)
☐	☒	For null hypothesis testing, the test statistic (e.g. *F*, *t*, *r*) with confidence intervals, effect sizes, degrees of freedom and *P* value noted *Give P values as exact values whenever suitable.*
☒	☐	For Bayesian analysis, information on the choice of priors and Markov chain Monte Carlo settings
☒	☐	For hierarchical and complex designs, identification of the appropriate level for tests and full reporting of outcomes
☒	☐	Estimates of effect sizes (e.g. Cohen's *d*, Pearson's *r*), indicating how they were calculated

Our web collection on statistics for biologists contains articles on many of the points above.

Software and code

Policy information about availability of computer code

Data collection	Kinetic Monte Carlo simulations were performed using a custom code in C programming language. The source codes are available under https://doi.org/10.5281/zenodo.13950636. MD simulations were carried out with GROMACS. Input files (structures, topologies, parameter files, run-input files) as well as output files (pull positions and pull forces, final structures) required for reproducing our results are available at https://doi.org/10.5281/zenodo.13950636.
Data analysis	Experimental data were analyzed using GraphPad Prism Version 9. The data obtained by kinetic Monte Carlo simulations were analyzed using R. MD simulations were analyzed with GROMACS.

For manuscripts utilizing custom algorithms or software that are central to the research but not yet described in published literature, software must be made available to editors and reviewers. We strongly encourage code deposition in a community repository (e.g. GitHub). See the Nature Portfolio guidelines for submitting code & software for further information.

Data

Policy information about availability of data

All manuscripts must include a data availability statement. This statement should provide the following information, where applicable:

- Accession codes, unique identifiers, or web links for publicly available datasets
- A description of any restrictions on data availability
- For clinical datasets or third party data, please ensure that the statement adheres to our policy

All data needed to evaluate the conclusions in the paper are present in the paper and/or supporting information. The data that support the plots within this paper and other findings of this study are available on Zenodo under the DOI https://doi.org/10.5281/zenodo.13950636.

Research involving human participants, their data, or biological material

Policy information about studies with human participants or human data. See also policy information about sex, gender (identity/presentation), and sexual orientation and race, ethnicity and racism.

Reporting on sex and gender	*Use the terms sex (biological attribute) and gender (shaped by social and cultural circumstances) carefully in order to avoid confusing both terms. Indicate if findings apply to only one sex or gender; describe whether sex and gender were considered in study design; whether sex and/or gender was determined based on self-reporting or assigned and methods used.* *Provide in the source data disaggregated sex and gender data, where this information has been collected, and if consent has been obtained for sharing of individual-level data; provide overall numbers in this Reporting Summary. Please state if this information has not been collected.* *Report sex- and gender-based analyses where performed, justify reasons for lack of sex- and gender-based analysis.*
Reporting on race, ethnicity, or other socially relevant groupings	*Please specify the socially constructed or socially relevant categorization variable(s) used in your manuscript and explain why they were used. Please note that such variables should not be used as proxies for other socially constructed/relevant variables (for example, race or ethnicity should not be used as a proxy for socioeconomic status).* *Provide clear definitions of the relevant terms used, how they were provided (by the participants/respondents, the researchers, or third parties), and the method(s) used to classify people into the different categories (e.g. self-report, census or administrative data, social media data, etc.)* *Please provide details about how you controlled for confounding variables in your analyses.*
Population characteristics	*Describe the covariate-relevant population characteristics of the human research participants (e.g. age, genotypic information, past and current diagnosis and treatment categories). If you filled out the behavioural & social sciences study design questions and have nothing to add here, write "See above."*
Recruitment	*Describe how participants were recruited. Outline any potential self-selection bias or other biases that may be present and how these are likely to impact results.*
Ethics oversight	*Identify the organization(s) that approved the study protocol.*

Note that full information on the approval of the study protocol must also be provided in the manuscript.

Field-specific reporting

Please select the one below that is the best fit for your research. If you are not sure, read the appropriate sections before making your selection.

☒ Life sciences ☐ Behavioural & social sciences ☐ Ecological, evolutionary & environmental sciences

For a reference copy of the document with all sections, see nature.com/documents/nr-reporting-summary-flat.pdf

Life sciences study design

All studies must disclose on these points even when the disclosure is negative.

Sample size	We used standard methods for data analysis and statistical testing as described in the main text and methods. Samples sizes are indicated for each figure in the figure legend.
Data exclusions	No data exclusions.
Replication	All in vitro experiments were repeated at least three times.
Randomization	N/A
Blinding	Data collection and analysis were performed by the same investigators (see list of author contributions).

Reporting for specific materials, systems and methods

We require information from authors about some types of materials, experimental systems and methods used in many studies. Here, indicate whether each material, system or method listed is relevant to your study. If you are not sure if a list item applies to your research, read the appropriate section before selecting a response.

Materials & experimental systems

n/a	Involved in the study
☒	☐ Antibodies
☒	☐ Eukaryotic cell lines
☒	☐ Palaeontology and archaeology
☒	☐ Animals and other organisms
☒	☐ Clinical data
☒	☐ Dual use research of concern
☒	☐ Plants

Methods

n/a	Involved in the study
☒	☐ ChIP-seq
☒	☐ Flow cytometry
☒	☐ MRI-based neuroimaging

Plants

Seed stocks

Report on the source of all seed stocks or other plant material used. If applicable, state the seed stock centre and catalogue number. If plant specimens were collected from the field, describe the collection location, date and sampling procedures.

Novel plant genotypes

Describe the methods by which all novel plant genotypes were produced. This includes those generated by transgenic approaches, gene editing, chemical/radiation-based mutagenesis and hybridization. For transgenic lines, describe the transformation method, the number of independent lines analyzed and the generation upon which experiments were performed. For gene-edited lines, describe the editor used, the endogenous sequence targeted for editing, the targeting guide RNA sequence (if applicable) and how the editor was applied.

Authentication

Describe any authentication procedures for each seed stock used or novel genotype generated. Describe any experiments used to assess the effect of a mutation and, where applicable, how potential secondary effects (e.g. second site T-DNA insertions, mosiacism, off-target gene editing) were examined.